Hindawi
Advances in Materials Science and Engineering
Volume 2022, Article ID 7860273, 22 pages
https://doi.org/10.1155/2022/7860273

Research Article

Factors Influencing Piezoelectric Response of Horizontally and Vertically Embedded PZT Patch in Confined Granular Fills

Nisha Kumari[1] **and Ashutosh Trivedi**[2]

[1]*Research Scholar, Civil Engineering Department, Delhi Technological University, Delhi-110042, India*
[2]*Civil Engineering Department, Delhi Technological University, Delhi-11042, India*

Correspondence should be addressed to Nisha Kumari; nishasoni.ce@gmail.com

Received 7 March 2022; Revised 14 May 2022; Accepted 27 May 2022; Published 16 June 2022

Academic Editor: Wen-Shao Chang

The energy harvesting from ambient vibrations in the confined granular fill along the expressways and highways is a prospective power source for varied engineering applications. This paper presents the study of charge density, voltage output, and power from the *PZT* (lead zirconate titanate) patches embedded in dynamically loaded confined granular fill. The effect of the alignment of *PZT* patches, thickness ratio, material properties of the confined granular fill, and retaining structure on the voltage output is investigated. It provides the scope for the evaluation of voltage output directly from the stress-strain response, position of the *PZT* patch, and the engineering properties of the confined granular fill. The alignment of *PZT* patches in the horizontal and vertical directions has been examined analytically to optimize voltage outputs. The results indicate that the modulus ratio of the material, alignment of *PZT* patches, and gradation of infill material significantly affect the voltage generation. A relationship for voltage and power output has been proposed for a set of engineering applications. The observed voltage output is found appropriate for wide-ranging implements classified as low- (LRA), medium- (MRA), and high- (HRA) resistance applications. It is proposed to be up-scaled using multiple patches embedded throughout the confined granular fill and pavements subjected to continuous dynamic loads.

1. Introduction

The dynamically loaded transportation infrastructures find a unique application for energy harvesting and structural health monitoring due to the profound developments in sensor technology. This energy can be captured using a suitable mechanism for various micro- and macro-engineering operations, including electrical devices and transportation as a renewable energy system [1]. The piezoelectric material provides higher energy density and flexibility in being integrated into a system than the electromagnetic and electrostatic units [2, 3]. Many researchers [4–6] have analysed the effectiveness of embedded *PZT* (lead zirconate titanate) patches for energy harvesting and health monitoring structures.

Many studies [7–9] considered vibration-based energy harvesting using piezoelectric material for civil infrastructure systems due to dynamic loads of traffic movements. An analytical expression has been proposed for a small *PZT* patch attached to the surface of a bridge structure. The Hamiltonian principle was considered to account for all the vibration modes of the structure and pointed out that the surface strain fluctuations influence voltage output [10]. The electrical energy generation was investigated in a prestressed tuneable piezoelectric beam harvester from a bridge's vibrations under ambient loading conditions [11]. They concluded that the maximum power generation from the *PZT* patch is a function of the excitation frequency of the dynamic loads. Experimental validation for a rail bridge in their operational condition for energy harvesting from the random vibrations of the built infrastructure within the laboratory environment was presented where the theoretical predictions were less than the experimental output [12]. The feasibility of energy harvesting from friction-induced vibration was associated with stronger vibrations [13]. A few researchers [14, 15] have analysed the performance and structural response of the pavement with an embedded piezoelectric energy harvester. The structural response of the asphalt pavement embedded with a piezoelectric energy harvester (PEH) provided a couple of optimization solutions for design [16]. Table 1 presents a brief review of specific power production capabilities of alternative energy harvesting sources, including *PZT* patches. It shows the vast potential of *PZT* patches for various micro- and macro-engineering operations.

Few investigators performed field observation for the piezoelectric cantilever installed above the pavement and embedded underground [17]. They found that a significant amount of electrical energy is generated from the embedded piezoelectric cantilever. The stress on the surface influences the piezoelectric effect of the PZT patches. The voltage polarization of the *PZT* patch is significantly affected by its embedment depth and orientation. It was found that the vertical compressive stress is decreased when depth is increased effectively [18]. The performance of the *PZT* patches for energy harvesting from the pavement combines the stiffness and load pattern. Comparing the impact of the dynamic loads, the influence of the pavement thickness on the power generation is negligible [19].

The literature review indicates that the application of piezoelectric material in civil structures is an abundant source of energy. The existing experimental and numerical analysis usually focuses on the methods of piezoelectric energy from various structural elements, namely beams, bridges, roads, and rail tracks. By contrast, there are no significant studies on the stress response of confined granular fill on power generation due to vibrations. The *PZT* patches embedded in the pavement undergo reversal in the voltage polarity for both horizontal and vertical faces [18]. Therefore, the piezoelectric power output is not necessarily higher for the stronger vibrations. The power output depends on the magnitude of strain generation due to vertical and horizontal vibrations. From previous analytical studies [18, 38], it appears that the resultant vertical stresses and horizontal stresses are affected by the placement of the *PZT* patch on the retaining face compared to the horizontal pavement structure. Similar observations were made [39] for the increasing depth of embedment of the *PZT* patch. The analytical study helps us to identify the set of design parameters that can improve the efficiency of the piezoelectric energy output. The efficiency of charge output depends upon the magnitude of the force excitation, the material characteristics, and the electromechanical coupling of the piezoelectric material structure [40, 41]. The piezoelectric response of the *PZT* patch can be optimized by changing the mechanical properties through variation in the modulus [42].

The objective of this study is a parametric investigation of the factors influencing the piezoelectric voltage generation considering the installation position of the *PZT* patch, and geometric and mechanical properties of the embedded *PZT* patch in confined granular fill. The confined granular fill is contained by the pavement and the retaining structure. The confined granular fill experiences vibrations due to dynamic loads. The strain fluctuation is absorbed by the *PZT* patch, which polarized and induced a voltage. This deformation per unit length is analysed by the stress-strain response of the confined granular fill due to the ambient vibration. The deformation of the *PZT* patch is used to calculate the charge density and voltage output. The model that consists of confined granular fill with embedded *PZT* patches is analysed theoretically. The electromechanical process is used to convert mechanical energy into electrical energy. The charge density and voltage output from the *PZT* patch are discussed with a focus on the influence of the embedded position, piezoelectric properties, geometric properties of the *PZT* patch, and confined granular fill.

The present study evaluates the charge density and voltage output over the permittivity, placement of the *PZT* patch, depth of embedment, and geometric properties of the retaining structure. Figure 1 shows a flow chart of the conversion of mechanical energy into electrical energy from the confined granular fill. The mechanical vibration of dynamic loads for energy harvesting consists of a loading system, which transfers the vibration waves through the mechanical units. The mechanical unit comprises a pavement with a *PZT* patch embedded horizontally and vertically over the granular fill retained by a retaining wall. Besides the energy generation, the influence of the material properties on the polarization of the *PZT* patch is a vital engineering parameter influencing charge density.

The results show the geometric properties of the retaining structure and mounted position of the *PZT* patch on the transformation of mechanical into electrical energy through the change in charge density and voltage output. It has been demonstrated that the piezoelectric response of a *PZT* patch embedded in the confined granular fill can be tuned through the changes in its thickness and stiffness. A comparison of output voltage among the hard, semihard, and soft *PZT* patches based on piezoelectric material properties has been made. Based on the theoretical analysis, the influence of different alignments and stiffness of the *PZT* patch on the output energy is captured.

2. Engineering Properties of *PZT* Patches

When piezoelectric materials are subjected to mechanical stress, electrical energy generated in proportion to that stress is known as the direct piezoelectric effect. The direct effect occurs through the compression of piezoelectric material, as shown in Figure 2. D_3 is the electric displacement on the *PZT* patch, E_3 is the electric field in direction-3, d_{31} is the piezoelectric strain coefficient in mode 31, ε_{33}^{T} represents the permittivity of the material in the direction-33 under conditions of constant mechanical stress ($\varepsilon_{33}^{T=0}$ corresponds to free permittivity), and σ_{PZT} is stress in the *PZT* layer.

Piezoelectric energy output is commonly based on two coupling modes: 33-mode and 31-mode, as shown in Figures 3–4. The coupling mode defines the capability of piezoelectric material to transform mechanical energy into electrical energy. Figure 3 shows a 33-mode *PZT* patch where the external stress direction generated an electric field in the same direction. Figure 4 shows 31-mode where the applied

Table 1: Energy output capacities of varied system configurations.

System configuration	Energy output	Estimated cost
Typically a dynamic loading from the busy expressway[a]	188 kW	$0.08-$0.18/kWh
PZT system paved in roadway section with very high traffic volume[b]	4.04 MWh	$1.77/kWh
Fan-typed windmill using induced resonance[c]	613 μW	—
Piezoelectric cantilever embedded in small fan windmill[d]	363 μW	—
Aero-elastic energy harvesting using the piezoelectric transducer from wind tunnel[e]	27mw	—
Dynamic loading from the ocean waves[f]	60–180mw	—
Hydraulic pressure in the hydraulic systems[g]	1.2 mW	—
High-rise buildings due to wind and earthquake[h]	432.21 MW	—
Building due to pedestrian traffic[i]	1.1 MWh	$3850/per tile
A vibration-based system installed on bridge cable[j]	35.67 mW	$80-$85/kWh
Electromagnetic energy harvester from low-frequency mechanical vibrations[k]	554.7 μW	—
Electromagnetic generator utilized the low ambient vibrations[l]	46 μW	—
Oscillation motion of human body and vibration of machines[m]	95 mW	—
Power generation utilizing the vibration of moving cars[n]	3.9 mW	—
Pavement system supported by solar panels[o]	1718 MW	$0.05-$0.075/kWh
PV panels mounted 33-bus distribution network[p]	14 KW	—
Households and village power stations[q]	200–2500 W	$10-$12/W
Photovoltaic noise barriers with motorways and railway tracks[r]	800 MWh	—

[a]Hill et al. [20]; [b]Guo and Lu [21]; [c]Yang et al. [22]; [d]Rezaei-Hosseinabadi et al. [23]; [e]Sousa et al. [24]; [f]Murray and Rastegar [25]; [g]Cunefare et al. [26]; [h]Xie et al. [27]; [i]Li and Strezov [28]; [j]Kim et al. [29]; [k]Zorlu et al. [30]; [l]Beeby et al. [31]; [m]Sasaki et al. [32]; [n]Glynne-Jones et al. [33]; [o]Wang et al. [34]; [p]Jiang et al. [35]; [q]Zahedi [36]; [r]Nordmann et al. [37].

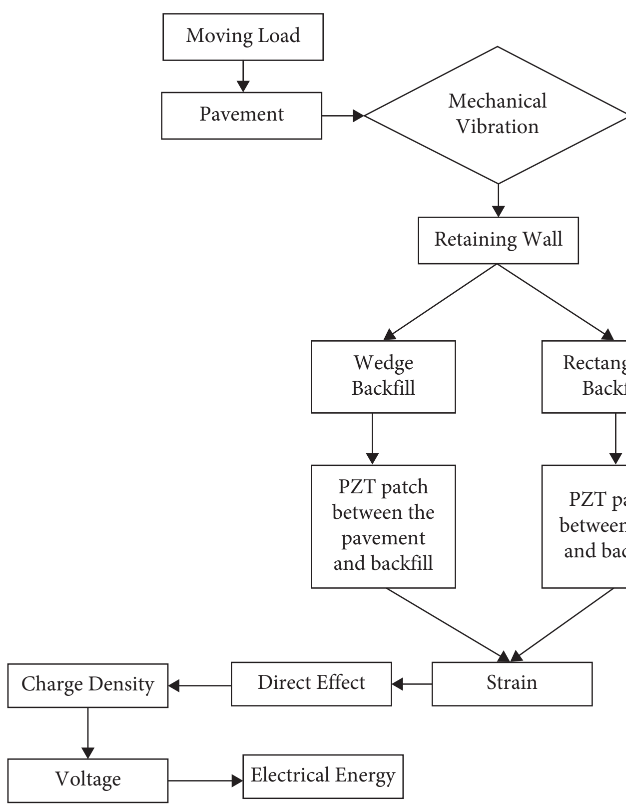

Figure 1: Flow chart for electromechanical energy output from mechanical vibrations.

stress is axial and perpendicular to the direction of the electric field.

The parameters influencing the voltage output from the PZT patches are relative permittivity ($\varepsilon_{33}^{T}/\varepsilon_o$) (here, ε_0 refers to the absolute permittivity of the vacuum), piezoelectric strain constant (d), polarization ratio (d_{31}/ε_{33}), and piezoelectric voltage coefficient (g). The charge density of the PZT patch is the most important consideration when choosing a piezoelectric material for energy harvesting. The product of the effective piezoelectric strain constant (d) and the effective piezoelectric voltage constant (g) determines the magnitude of the charge density [44]. The *PZT* material considerations are classified as the hard, semihard, and soft *PZT* patches, as shown in Table 2. The piezoelectric material considerations

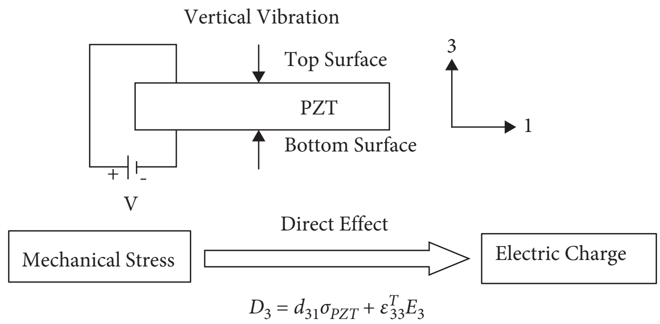

Figure 2: Flow chart for the generation of electric charge due to mechanical vibrations.

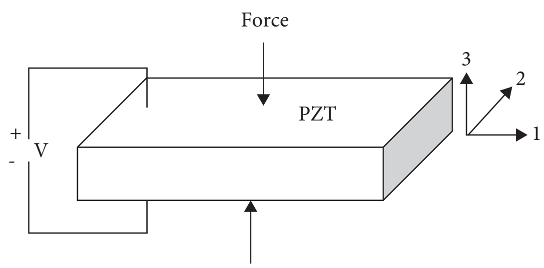

Figure 3: Mode of operation for the PZT patch (33-mode).

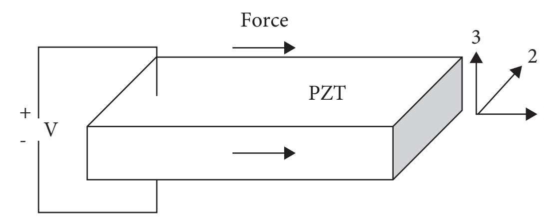

Figure 4: Mode of operation for the PZT patch (31-mode).

for engineering applications include piezoelectric strain constant, piezoelectric voltage constant, and mechanical quality factor (*Q*). The relative permittivity of the selected *PZT* patches (Table 2) was 1250, 1450, and 2400, while the polarization ratio was 0.112, 0.114, and 0.087, respectively. The polarization ratio is defined as the ratio of piezoelectric strain constant and relative permittivity.

2.1. Stress-Strain and Charge Density. The stress-strain response of the *PZT* patch embedded in the confined granular fill has been obtained in terms of charge density and voltage using a systematic numerical approach. The position of the *PZT* patch and its geometric properties influences the magnitude of deformation as described in the following sections.

2.2. Stress-Strain Behaviour. The stress-strain behaviour of the *PZT* patch has been considered for horizontal and vertical alignments. Initially, a *PZT* patch is horizontally and vertically embedded in the confined granular fill (Figure 5(a)). It has been assumed that the neutral plane of the *PZT* patch does not coincide with the geometrical centre of the fill. There is a negligible shear movement or separation among the retaining structure, *PZT* patch, and granular fill. The retaining structure is considered flexible and elastically constrained at the base. The shape of the useful part of the granular fill is considered a triangular wedge as shown in Figure 5(b). The vibrating system consists of a wall of height H, length L (such that $L = 1$), and backfill of thickness h_R. The thickness of *PZT* patch is h_p. As the result of the vibration, the stresses are generated in the pavement, granular fill, and *PZT* patch.

The deformation in the horizontally embedded *PZT* patch is a function of *PZT* material properties, bending moment, the width of backfill, modulus ratio, and thickness ratio (Appendix A). The strain in the horizontally embedded *PZT* patch [45] is expressed as

$$\varepsilon_{HE} = f\left(M, b_S, E_s, h_R, \mu, n\right) = \frac{36M}{b_S E_S h_R^2}\left[\frac{(1+\mu)(1+\mu n)}{3\mu^5 n^3 + 6\mu^4 n^2 + 5\mu^3 n + \mu^2 n^2 + \mu^2 + 4\mu n + 2}\right]. \quad (1)$$

The stress in the horizontally embedded patch is a function of strain and modulus of the *PZT* and is expressed as

$$\sigma_{HE} = \varepsilon_{HE} * E_P = \frac{36M}{b_S h_R^2}\left[\frac{n(1+\mu)(1+\mu n)}{3\mu^5 n^3 + 6\mu^4 n^2 + 5\mu^3 n + \mu^2 n^2 + \mu^2 + 4\mu n + 2}\right], \quad (2)$$

Table 2: Engineering properties of piezoelectric patches.

Engineering properties	Symbol	Hard patch; PZT-141	Semihard; PZT-155	Soft patch; PZT-151
Density (kg/m^3)	ρ	7800	7800	7800
Modulus of PZT patch (GPa)	E_P	81	63	60
Relative permittivity[a]	$\varepsilon_{33}^T/\varepsilon_o$	1250	1450	2400
Dielectric loss factor[a]	tan δ	5×10^{-3}	20×10^{-3}	20×10^{-3}
Piezoelectric strain constant[a] (C/N)	d_{31}	-140×10^{-12}	-165×10^{-12}	-210×10^{-12}
	d_{33}	310×10^{-12}	360×10^{-12}	500×10^{-12}
Piezoelectric voltage coefficient[a] (Vm/N)	g_{31}	-13.1×10^{-3}	12.9×10^{-3}	-11.5×10^{-3}
	g_{33}	29×10^{-3}	27×10^{-3}	22×10^{-3}
Polarization ratio[b]	d_{31}/ε_{33}	0.112	0.114	0.087

[a]Physik Instrumente GmbH [43]; [b]present work.

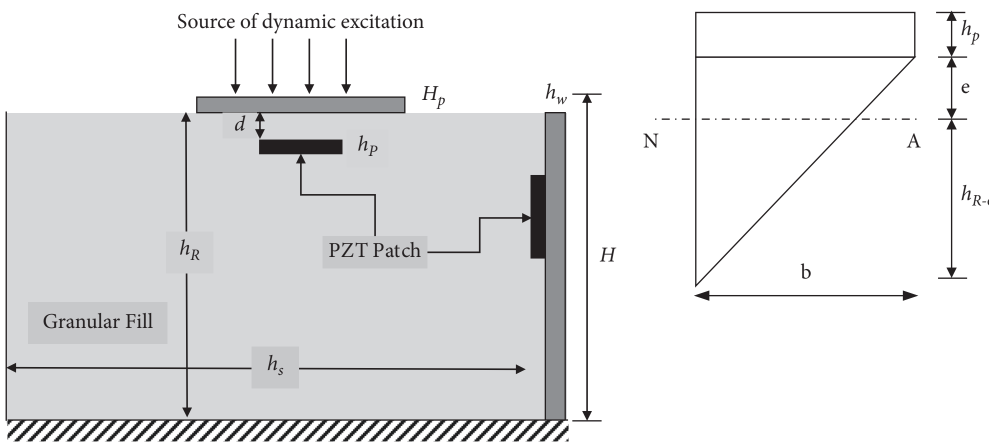

Figure 5: (a) PZT patch of the thickness (h_P) horizontally and vertically embedded in the confined granular fill of thickness (h_R) retained by retaining structure of height (H). (b) Cross section of the triangular wedge with PZT patch.

where ε_{HE} and σ_{HE} are the strain and the stress in a horizontally embedded *PZT* patch. E_S and E_P are Young's modulus of backfill and PZT patch, respectively; μ is the ratio of the thickness of the *PZT* patch to the backfill h_P/h_R; and n is the ratio of the modulus of the *PZT* patch to the backfill (E_P/E_R), and M is the bending moment *PZT* patch.

The strain in the vertically embedded *PZT* patch is the function of bending moment, the height of the retaining structure, modulus ratio, height of the backfill, and thickness ratio [46] is expressed as

$$\varepsilon_{VE} = \int (M, H, h_S, a, b, \mu, n) = \frac{36M}{E_s H h_s^2}\left[\frac{\left(3\mu + 2 - 12a^2 b\mu^2 n\right)[24\mu n(a+b)+1]}{\left[3n\mu^3\left(1+ba^3\right)+1\right][24\mu n(a+b)+1]^2 + 18\left(3\mu+2-12a^2b\mu^2n\right)[2\mu n(1+ab)+1]}\right]. \tag{3}$$

Similarly, the stress for vertically embedded *PZT* patch between the granular fill and retaining wall is expressed as

$$\sigma_{VE} = \varepsilon_{VE} * E_P = \frac{36nM}{H h_s^2}\left[\frac{\left(3\mu + 2 - 12a^2 b\mu^2 n\right)[24\mu n(a+b)+1]}{\left[3n\mu^3\left(1+ba^3\right)+1\right][24\mu n(a+b)+1]^2 + 18\left(3\mu+2-12a^2b\mu^2n\right)[2\mu n(1+ab)+1]}\right], \tag{4}$$

where ε_{VE} and σ_{VE} are the strain and stress in vertically embedded *PZT* patch, a is the thickness ratio of retaining wall and *PZT* patch (h_w/h_P), and b is the modulus ratio of retaining wall and *PZT* patch (E_w/E_P).

2.3. Charge Density for the Horizontally Embedded PZT Patch. The charge density equations for the hard, semihard, and soft *PZT* patches embedded horizontally have been derived from the stress-strain relationship of the *PZT* patch subject to vibrations in the confined granular fill. A single layer of *PZT* patch horizontally embedded between the pavement and the granular fill is shown in Figure 5(a). The deflection induces curvature in the triangular wedge at an arbitrary point on the neutral axis due to bending. The power output and the dynamic response of the piezoelectric system entirely depend on the coupling mode of the PZT patch. The researchers [47, 48] have identified that the natural way of excitation of retaining structure is in d_{31} mode. Therefore, the d_{31} mode has been chosen in the present work for analysis. For the so configured system, the tensorial representation of the piezoelectric constitutive equation [49] gives the electric displacement as

$$D_3 = d_{31}\sigma_{PZT} + \varepsilon_{33}^{T}E_3. \tag{5}$$

The stress generated in the *PZT* patch due to the dynamic loads on the confined granular fill changes the polarization and the displacement on the upper and lower surface of the *PZT* patch. As there is no external electric source ($E_3 = 0$), the electric displacement in the *PZT* patch is expressed as

$$D_3 = d_{31}\sigma_{PZT}. \tag{6}$$

The charge density function at the top and bottom surfaces of the horizontally embedded *PZT* patch is expressed as

$$\rho_{\mathrm{THE}} = D_3\left(Z, h_p + \frac{h_R}{3}\right), \tag{7}$$

$$\rho_{\mathrm{BHE}} = D_3\left(Z, h_P\right), \tag{8}$$

where ρ_{THE} and ρ_{BHE} are charge density functions at the top and bottom surfaces of the horizontally embedded *PZT* patch, respectively, and D_3 is electric displacement according to the piezoelectric coupling constitutive equation, and Z is the thickness direction coordinate from the neutral plane as shown in Figure 5(b).

From equations (6) and (7), the charge density is expressed as

$$Q_{\mathrm{THE}} = d_{31}\int_0^{\left(h_P+\left(h_R/3\right)\right)} \sigma_B \mathrm{d}z, \tag{9}$$

$$Q_{\mathrm{THE}} = \frac{12 d_{31} M}{b h_R}\left[\frac{n(1+\mu)(1+\mu n)(3\mu+1)}{3\mu^5 n^3 + 6\mu^4 n^2 + 5\mu^3 n + \mu^2 n^2 + \mu^2 + 4\mu n + 2}\right], \tag{10}$$

$$Q_{\mathrm{BHE}} = -d_{31}\int_0^{\left(h_p\right)} \sigma_B \mathrm{d}z, \tag{11}$$

$$Q_{\mathrm{BHE}} = \frac{-12 d_{31} M}{b h_R}\left[\frac{n\mu(1+\mu)(1+\mu n)}{3\mu^5 n^3 + 6\mu^4 n^2 + 5\mu^3 n + \mu^2 n^2 + \mu^2 + 4\mu n + 2}\right]. \tag{12}$$

The negative sign represents the opposite charge of the top surface, while Q_{THE} and Q_{BHE} are the charge density at the top and bottom surfaces of the horizontally embedded *PZT* patch, respectively.

2.4. Charge Density for the Vertically Embedded PZT Patch. The charge density determines the dipole mobility of the charges on the *PZT* surface and affects the efficiency of power generation. The charge density function at the top and bottom surfaces of the vertically embedded *PZT* patch is expressed as

$$\rho_{TVE} = D_3\left(Z, h_p + e\right), \tag{13}$$

where e is the distance between the bottom surface of *PZT* and the centre of gravity of the granular backfill, and is expressed as

$$e = \frac{h_P\left[6a + 1 - 6a^2\right]}{18a + 12}, \tag{14}$$

$$\rho_{BVE} = D_3\left(Z, h_p\right), \tag{15}$$

where ρ_{TVE} and ρ_{BVE} are the charge density function at the top and bottom surfaces of the vertically embedded *PZT* patch in the confined granular fill, h_p is the thickness of the *PZT* patch, a is the thickness ratio of the retaining wall and the *PZT* patch (h_w/h_P), D_3 is electric displacement according to the constitutive equation of the piezoelectric coupling, Z is the thickness direction coordinate from the neutral plane, and e is the distance between the neutral plane and bottom surface of the *PZT* patch as shown in Figure 5(b).

The charge density (equations (13) and (14)) is expressed as

$$Q_{\mathrm{TVE}} = d_{31} \int_{0}^{(h_P+e)} \sigma_E \mathrm{d}z, \tag{16}$$

$$Q_{TVE} = \frac{36 d_{31} n M}{h a h_s} \left[\frac{\left(3\mu + 2 - 12a^2 b\mu^2 n\right)\left(24\mu n(a+b)+1\right)\left(6a+1-6a^2\right)}{(18a+12)\left[\left(3n\mu^2\left(1+ba^3\right)+1\right)\left(24\mu n(a+b)+1\right)^2 + 18\left(3\mu+2-12a^2 b\mu^2 n\right)\left(2\mu a(1+ab)+1\right)\right]} \right], \tag{17}$$

$$Q_{\mathrm{BVE}} = -d_{31} \int_{0}^{(e)} \sigma_E \mathrm{d}z, \tag{18}$$

$$Q_{\mathrm{BVE}} = \frac{-36 d_{31} n M}{h a h_s} \left[\frac{\left(3\mu + 2 - 12a^2 b\mu^2 n\right)\left(24\mu n(a+b)+1\right)\left(6a^2+12a+11\right)}{(18a+12)\left[\left(3n\mu^2\left(1+ba^3\right)+1\right)\left(24\mu n(a+b)+1\right)^2 + 18\left(3\mu+2-12a^2 b\mu^2 n\right)\left(2\mu a(1+ab)+1\right)\right]} \right]. \tag{19}$$

Q_{TVE} and Q_{BVE} are the generated charge density at the top and bottom surfaces of the vertically embedded *PZT* patch, respectively.

2.5. Voltage Output for Horizontally and Vertically Embedded PZT Patches. Due to the phase difference, the charge developed at the opposite side of the *PZT* patch is collected by a separate electrode so that charge cancellation due to the phase difference in the electric displacement is prevented.

Since the charge quantity of the top and bottom surfaces is not the same, the voltage between the two poles is expressed as

$$V = \int_{e}^{(h_P+e)} E(x,z)\mathrm{d}z, \tag{20}$$

$$E = \frac{d_{31}\sigma_P}{\varepsilon_{33}}. \tag{21}$$

where V is the voltage between the top and bottom surfaces of the PZT patch due to vibration of the system, E is the equivalent electric field intensity, σ_P is stress in the PZT patch, and $\varepsilon_{33}^T/\varepsilon_o$ is relative permittivity. For a horizontally embedded PZT patch, the voltage output between the top and bottom surfaces of the PZT patch is expressed as

$$V_{HE} = \frac{h_R^2 d_{31} E_P \mu(3\mu+2)}{12\varepsilon_{33}\rho}, \tag{22}$$

$$V_{HE} = \frac{3Md_{31}}{b\varepsilon_{33}} \left[\frac{n\mu(1+\mu)(1+\mu n)(2+3\mu)}{3\mu^5 n^3 + 6\mu^4 n^2 + 5\mu^3 n + \mu^2 n^2 + \mu^2 + 4\mu n + 2} \right], \tag{23}$$

where V_{HE} is the voltage output for a horizontally embedded *PZT* patch in confined granular fill, d_{31} is the piezoelectric strain constant for 31-mode, and E_P is the elastic modulus of the *PZT* patch. Similarly, for a vertically embedded *PZT* patch, the voltage output between the top and bottom surfaces of the *PZT* patch is expressed as

$$V_{VE} = \frac{h_P^2 d_{31}\varepsilon_o E_P \mu^2\left(-6a^2+15a+13\right)}{2\varepsilon_{33}\rho(18a+12)}, \tag{24}$$

$$V_{VE} = \frac{18n\varepsilon_o M d_{31}}{H\varepsilon_{33}} \left[\frac{\mu^2\left(3\mu+2-12a^2 b\mu^2 n\right)\left(24\mu n(a+b)+1\right)\left(-6a^2+15a+13\right)}{18a+12\left[\left(3n\mu^3\left(1+ba^3\right)+1\right)\left(24\mu n(a+b)+1\right)^2 + 18\left(3\mu+2-12a^2 b\mu^2 n\right)\left(2\mu n(1+ab)+1\right)\right]} \right], \tag{25}$$

where V_{VE} is the voltage output of vertically embedded *PZT* patch, H is the height of the retaining structure, a and b denote the thickness ratio of retaining wall with *PZT* patch and the modulus ratio of retaining wall with *PZT* patch, respectively.

3. Results and Discussion

This section provides the stress-response results on power generation from the ambient vibration in retaining the structure of height *(H)* with horizontally and vertically embedded *PZT* patches. The charge density and voltage output are obtained, which are significantly affected by the

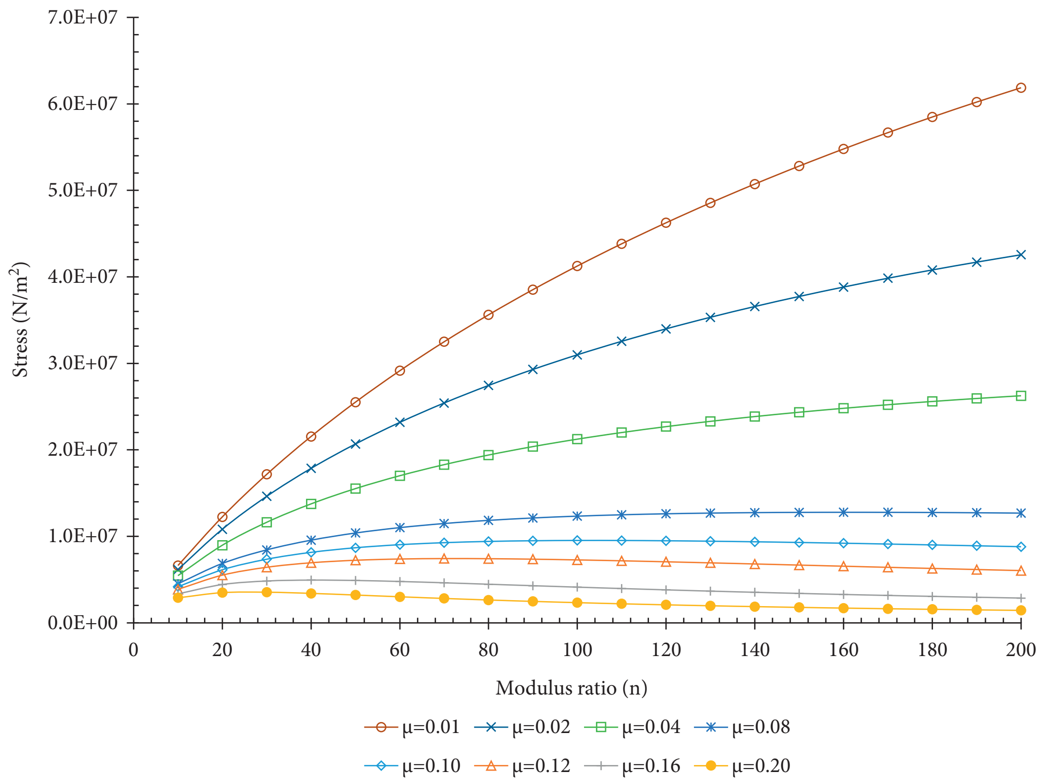

Figure 6: Stress variation with modulus ratio for the horizontally embedded PZT patch in confined granular fill computed for modulus ratio, the thickness of the backfill, the width of retaining structure, and thickness ratio.

stress state of the *PZT* patch. The stress-strain response of horizontally and vertically embedded *PZT* patches is analysed using equations (1)–(4). The effects of stiffness, polarization per unit permittivity, and geometric properties of the *PZT* patch have been obtained by equations (5)–(25). It is considered difficult to embed the *PZT* on the upper surface of the pavement (environmental, abrasion, and iteration effects). Therefore, it is recommended to embed the *PZT* at depth (d). Accordingly, the stiffness of the base course layer has been considered as 1–4 GPa [39]. The resilient modulus of hardened concrete is reported in the range of 10–30 GPa, while that of aggregate is between 45 and 85 GPa. Hence, the range of values (1–5 GPa), which are well below the hardened concrete, is used in this study.

The strain on the *PZT* patch is evaluated for varying thickness of the granular backfill. The comparative analysis is shown for varied piezoelectric materials, namely hard *(H)*, semihard *(SH)*, and soft *(S)* patches. To perform the technical analysis, the most commonly used parameters of the *PZT* patches, namely the relative permittivity ($\varepsilon_{33}^{T}/\varepsilon_{o}$), piezoelectric strain constant (d), piezoelectric voltage coefficient (g), and polarization ratio, are considered as mentioned in Table 2. The modulus of the *PZT* material varies with the temperature and thickness of the material. The researchers [50, 51] suggested that piezoelectric material has a stiffness of the order of 50–90 GPa. Therefore, to analyse the effect of the modulus ratio, the modulus of the hard, semihard, and soft *PZT* patch has been taken as 81, 63, and 60 GPa, respectively. The charge density and voltage output have been analysed for hard, semihard, and soft *PZT* patches.

4. Effect of Stiffness of Confined Granular Fill, Retaining Structure, and PZT Patch

The stiffness is the function of the geometry and the thickness of the material. The stress-strain response has been analysed by considering equations (2)–(4). Figure 6 shows the stress variation of the horizontally embedded *PZT* patch for varying thickness ratios considered in the range of $0.01 \leq \mu \leq 0.20$. The *PZT* patches are commercially available in a range of thicknesses from 0.20 to 20 mm (piezoelectric ceramic product 2011). The thickness ratio range is selected to capture the effect of the thickness of the *PZT* patch and granular fill. The thickness of the *PZT* patch was kept 10 mm while that of granular fill was 5–100 cm leading to a thickness ratio of 0.01 to 0.20.

From equation (16), it is observed that charge density is directly proportioned to the stress. Thus, the phenomenon indicates that the thickness of the retaining structure is a vital parameter for voltage output. Similarly, Figure 7 shows the stress response for the vertically embedded PZT patch for thickness ratio in the range of $0.01 \leq \mu \leq 0.20$. The negative values show the change in the nature of the stress. The change in sign indicates the compression and tension response of the stress. When a thin *PZT* patch has been embedded vertically, then the stress shows the opposite trend. It shows that the thickness of the surrounded granular

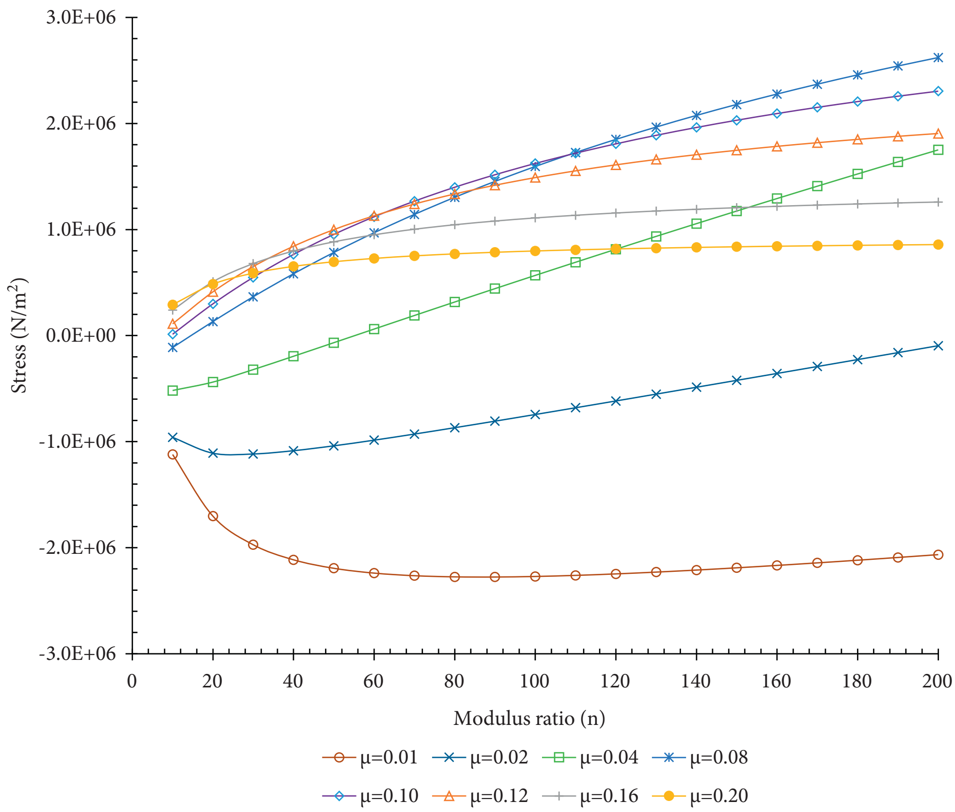

FIGURE 7: Stress variation with modulus ratio for the vertically embedded PZT patch in the confined granular fill computed for modulus ratio, the width of backfill, the width of retaining structure, and thickness ratio.

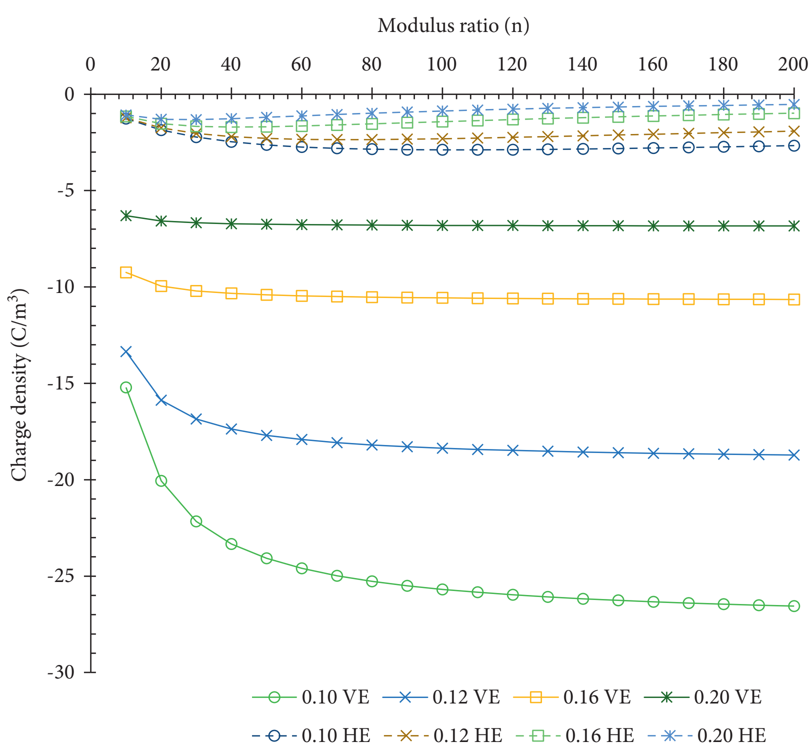

FIGURE 8: Charge density computed for retaining structure of unit width, piezoelectric strain, modulus ratio, and thickness ratio on the top surface of the horizontally and vertically embedded hard *PZT* patch in the confined granular fill.

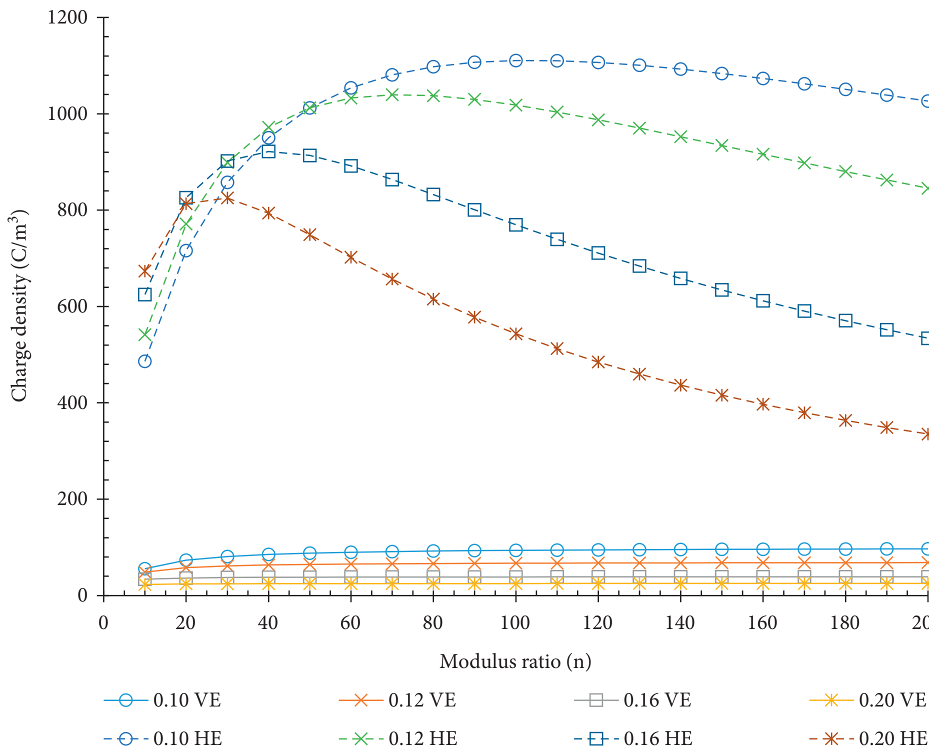

FIGURE 9: Charge density computed for retaining structure of unit width, piezoelectric strain, modulus ratio, and thickness ratio on the bottom surface of the horizontally and vertically embedded hard *PZT* patch in the confined granular fill.

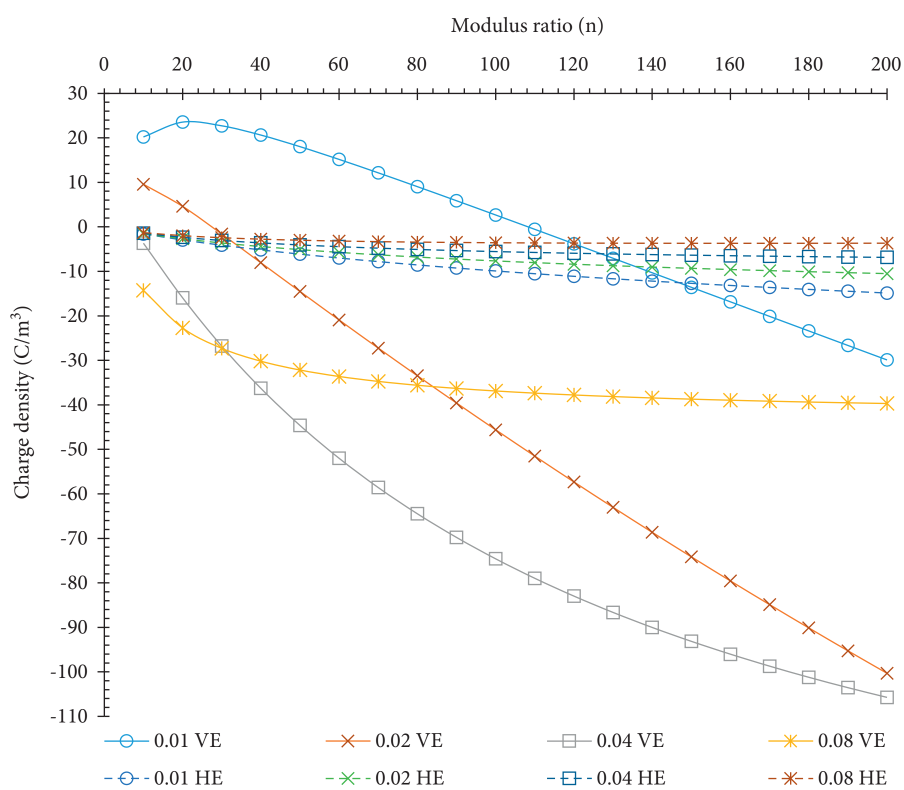

FIGURE 10: Charge density computed for retaining structure of unit width, piezoelectric strain, modulus ratio, and thickness ratio on the top surface of the horizontally embedded and from for vertically embedded hard *PZT* patch in the confined granular fill.

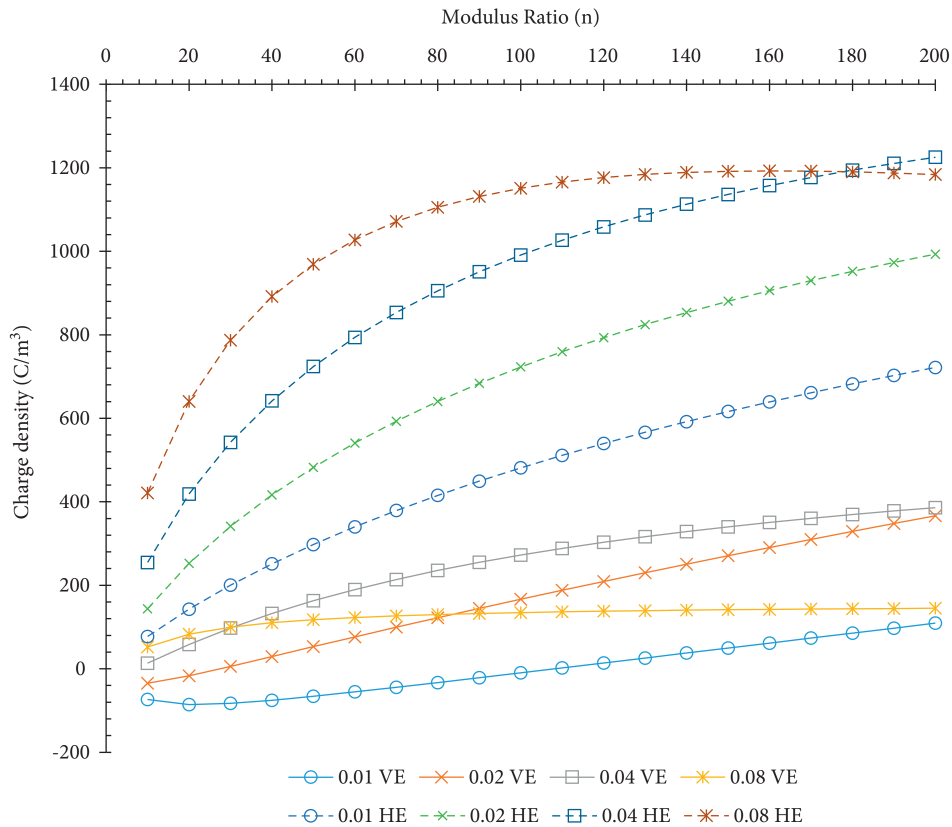

FIGURE 11: Charge density computed for retaining structure of unit width, piezoelectric strain, modulus ratio, and thickness ratio on the bottom surface of the horizontally and vertically embedded hard *PZT* patch in the confined granular fill.

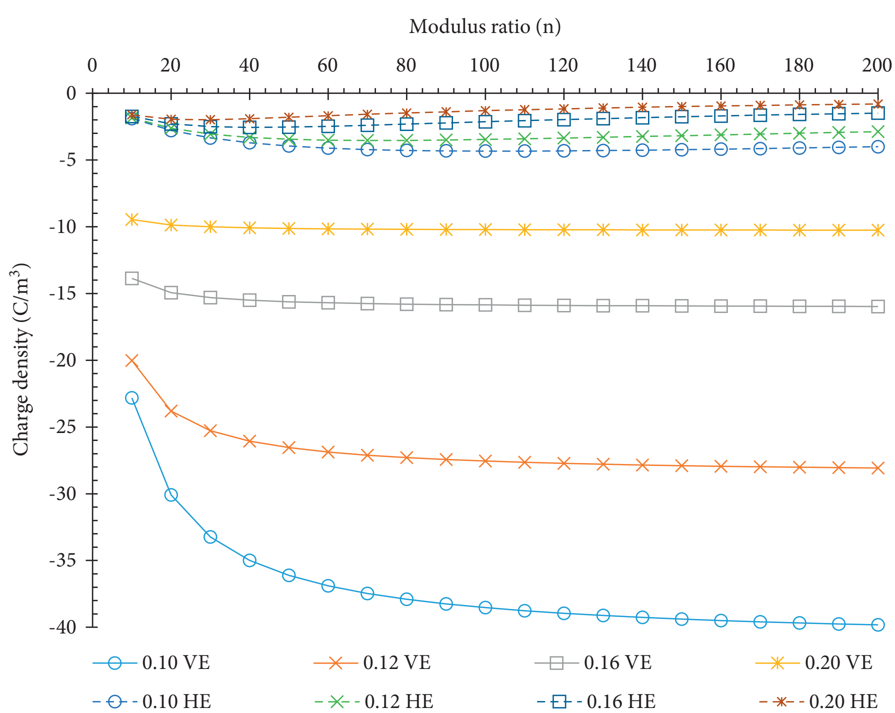

FIGURE 12: Charge density computed for retaining structure of unit width, piezoelectric strain, modulus ratio, and thickness ratio on the top surface of the horizontally and vertically embedded soft *PZT* patch in the confined granular fill.

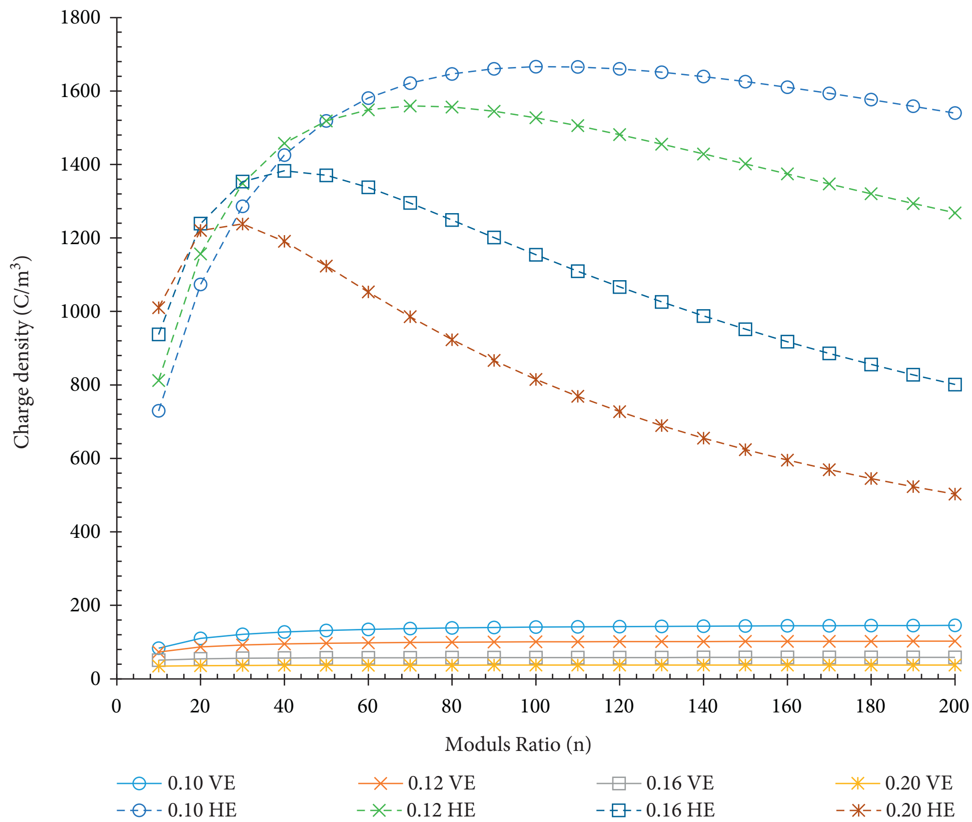

FIGURE 13: Charge density computed for retaining structure of unit width, piezoelectric strain, modulus ratio, and thickness ratio on the bottom surface of the horizontally and vertically embedded soft *PZT* patch in the confined granular fill.

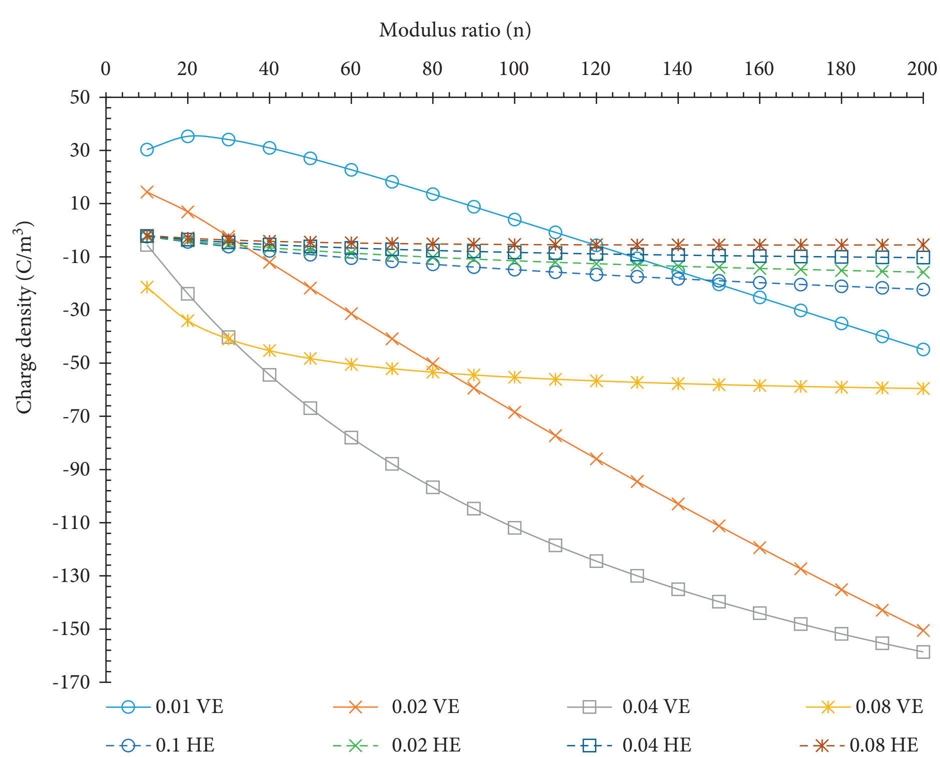

FIGURE 14: Charge density computed for retaining structure of unit width, piezoelectric strain, modulus ratio, and thickness ratio on the top surface of the horizontally and vertically embedded soft *PZT* patch in the confined granular fill.

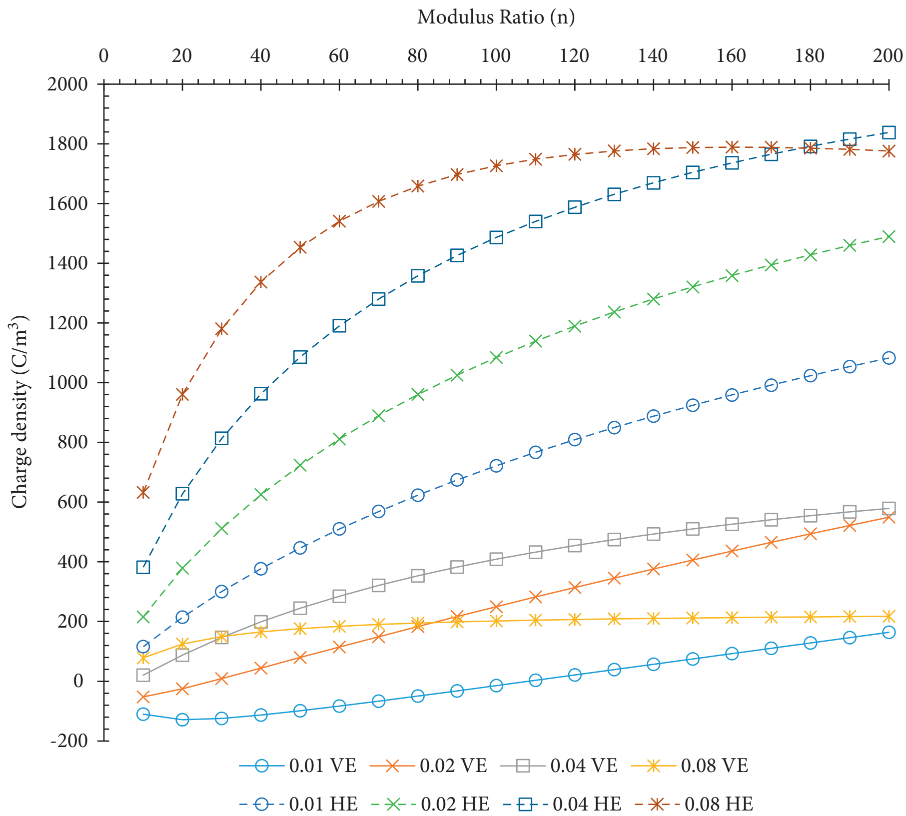

FIGURE 15: Charge density computed for retaining structure of unit width, piezoelectric strain, modulus ratio, and thickness ratio on the bottom surface of the horizontally and vertically embedded soft *PZT* patch in the confined granular fill.

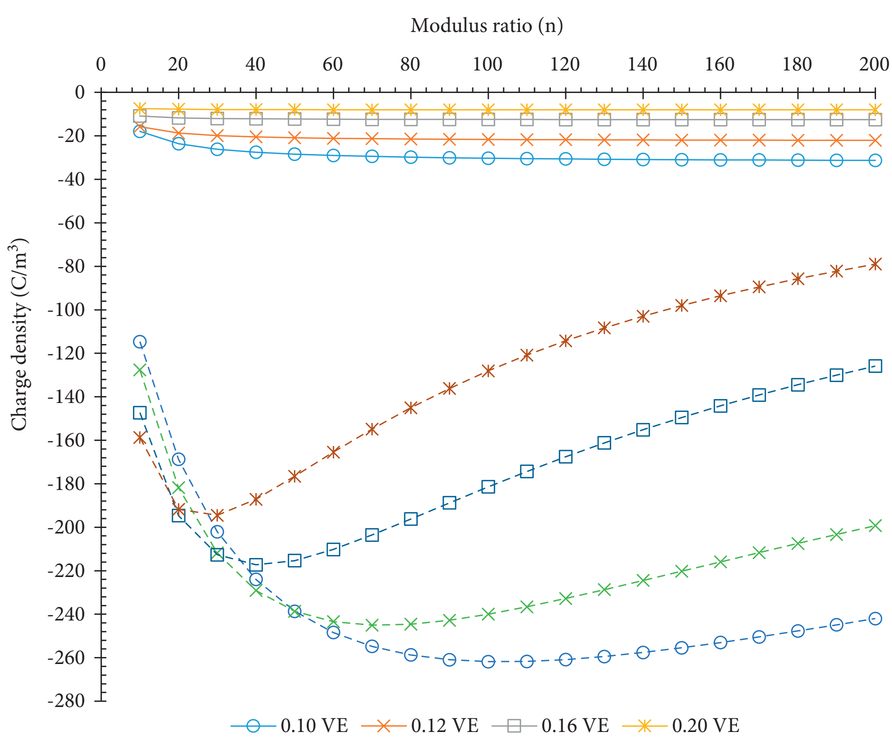

FIGURE 16: Charge density computed for retaining structure of unit width, piezoelectric strain, modulus ratio, and thickness ratio on the top surface of the horizontally and vertically embedded semihard *PZT* patch in the confined granular fill.

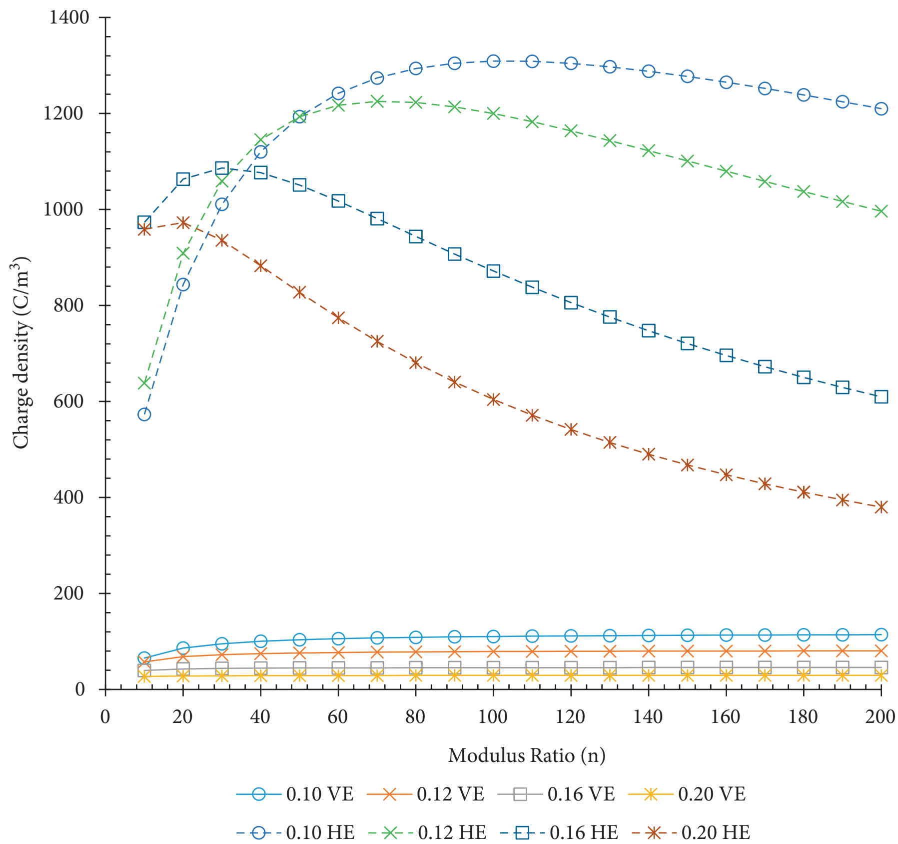

FIGURE 17: Charge density computed for retaining structure of unit width, piezoelectric strain, modulus ratio, and thickness ratio on the top surface of the horizontally and vertically embedded semihard *PZT* patch in the confined granular fill.

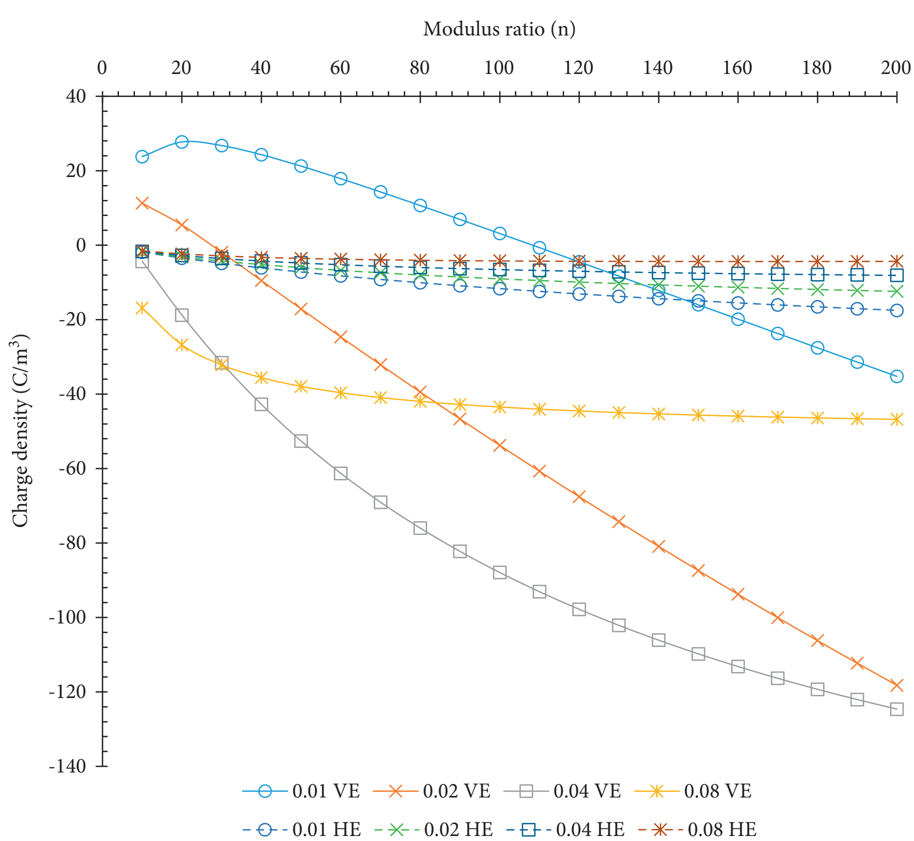

FIGURE 18: Charge density computed for retaining structure of unit width, piezoelectric strain, modulus ratio, and thickness ratio on the top surface of the horizontally and vertically embedded semihard *PZT* patch in the confined granular fill.

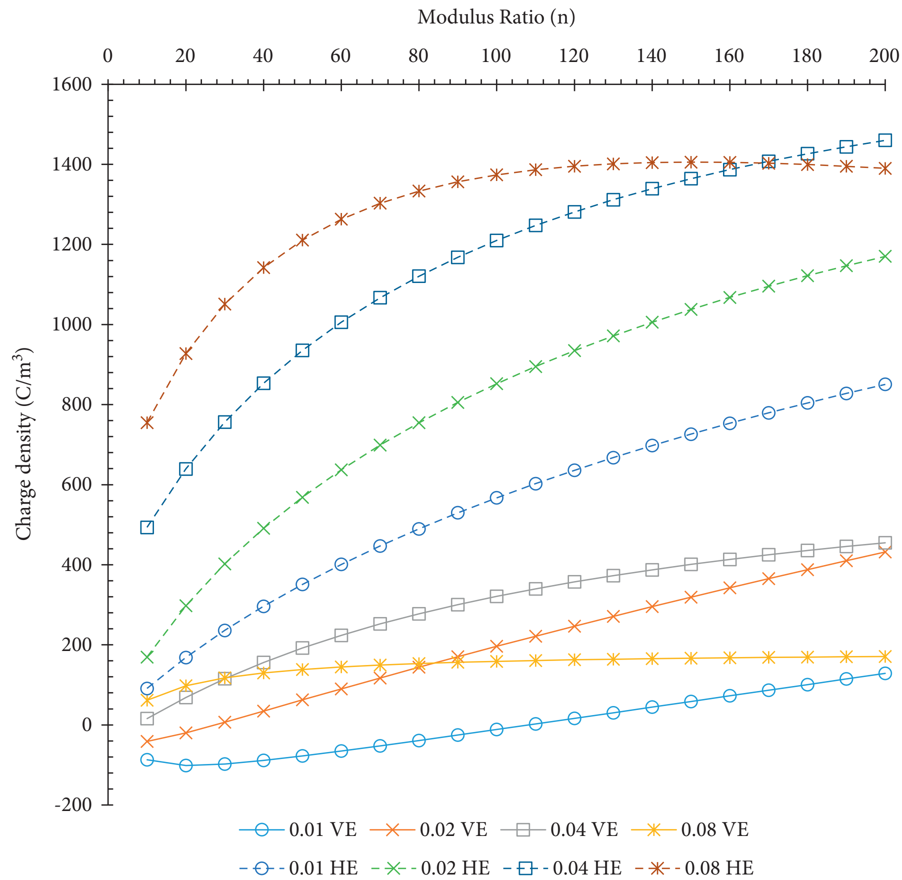

FIGURE 19: Charge density computed for retaining structure of unit width, piezoelectric strain, modulus ratio, and thickness ratio on the bottom surface of the horizontally and vertically embedded semihard *PZT* patch in the confined granular fill.

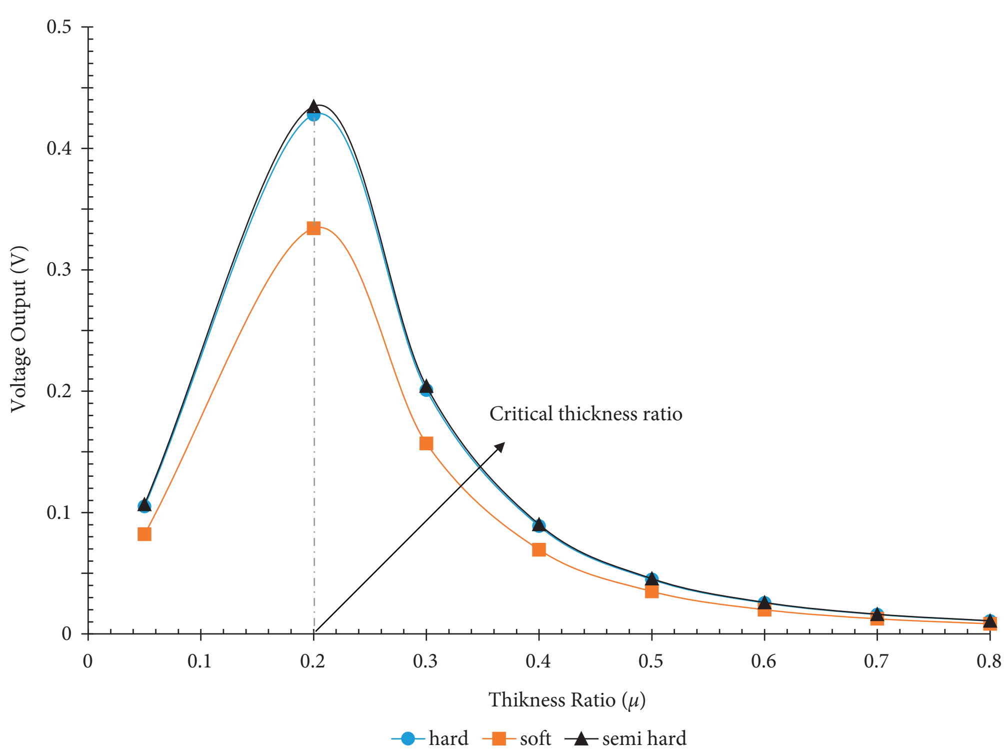

FIGURE 20: Voltage output computed for the retaining structure, piezoelectric strain constant, polarization ratio (0.112, 0.087, and 0.114), and thickness ratio of horizontally embedded hard, semihard, and soft PZT patch in the confined granular fill.

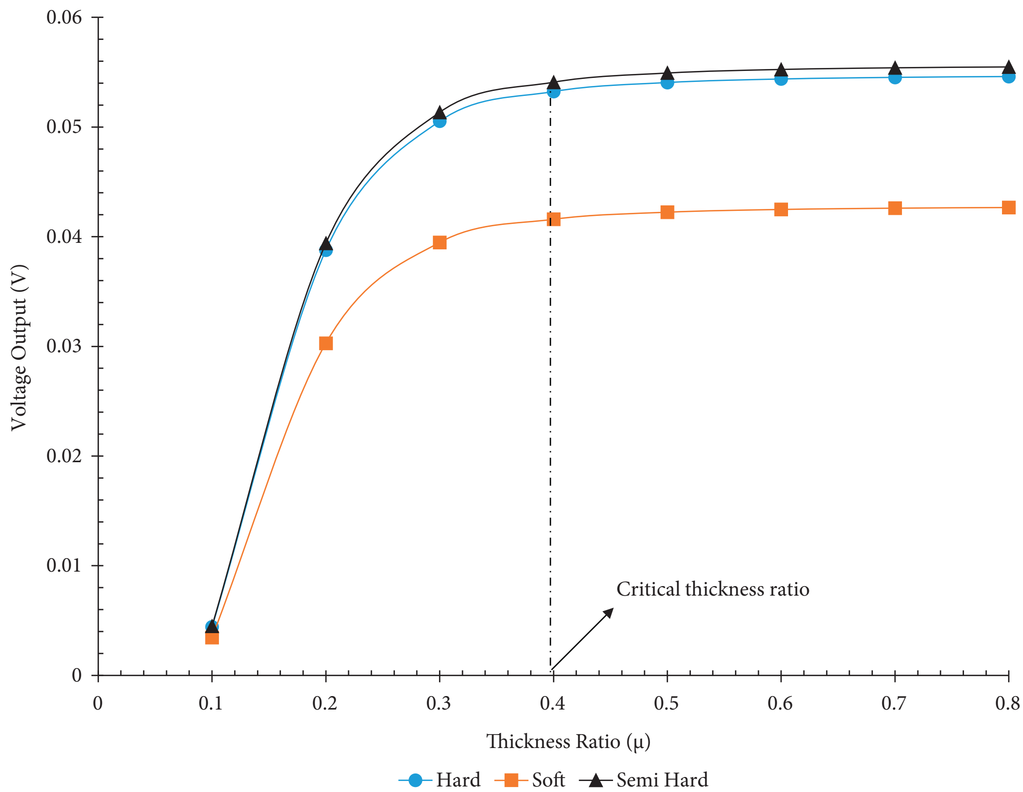

FIGURE 21: Voltage output computed for the retaining structure, piezoelectric strain constant, polarization ratio (0.112, 0.087, and 0.114) and thickness ratio of vertically embedded hard, semihard, and soft PZT patch in the confined granular fill.

fill affects the average stress in the *PZT* patch. This curve trend owes to the change in the distance between the centroid of the *PZT* patch and the neutral surface. Suppose the thickness ratio is reduced to 0.01. In that case, the maximum stress in the horizontally embedded *PZT* patch is more than five times higher than vertically embedded *PZT* patch. It has been observed that the thickness and material of the wall also affect the strain and stress behaviour of the confined granular fill (equation (4)).

4.1. Charge Density on Hard, Semihard, and Soft PZT Patches. A comparative study is presented for the hard (*H*), semihard (*SH*), and soft (*S*) *PZT* patches to capture the effect of geometric and mechanical parameters on the charge density on the *PZT* patch. The dominant parameters for the analysis are the installation position of the *PZT* patch, the thickness, and the modulus of the backfill material. The engineering properties of the *PZT* patch are shown in Table 2. As a result of the embedment of the *PZT* patch between the pavement and the granular material, the charge is induced on the top and on the bottom surface of the *PZT* patch. The difference between the positive and negative charges is proportional to the energy produced.

Figure 5(a) shows a physical model of the horizontally and vertically embedded *PZT* patch in the confined granular fill. The vibration in the backfill material deforms the horizontal embedded *PZT* patch. The piezoelectric phenomenon generates charge density on the surface of the *PZT* patch. Figures 8–19 show the variation of the charge density for the thickness ratios (μ) in the range of 0.10–0.20. Due to a small polarization ratio (0.114), the lowest charge is generated on the hard *PZT* patch as shown in Figures 8–11. The maximum charge is generated on the semihard (SH) patch as shown in Figures 16–19. Therefore, a semihard *PZT* patch is recommended as an effective piezoelectric material. The results also indicate that the energy efficiency of the output voltage is low for the loose granular fills.

For the vertically embedded *PZT* patch, the maximum charge is generated on the soft *PZT* patch as shown in Figures 12–15. For the thickness ratios (μ) in the range of 0.10–0.20, the results show that the total charge induced on the horizontally embedded *PZT* patch is higher than the vertically embedded patch. It indicates that the geometric parameters, modulus of granular fill, and wall significantly affect the charge density on the top and the bottom surface of the *PZT* patch (equations (17)–(19)).

Table 3 presents the maximum charge density on the top and bottom surfaces of the *PZT* patches for thickness ratios in the range of 0.01–0.08 and 0.10–0.20 based on the alignment of a patch.

4.2. Comparative Analysis of Voltage Output. In this section, the voltage output from different *PZT* patches is analysed by considering the variation of the stress-strain response (equations (20)–(25)). The key parameters influencing voltage output are the polarization, alignment of the *PZT*

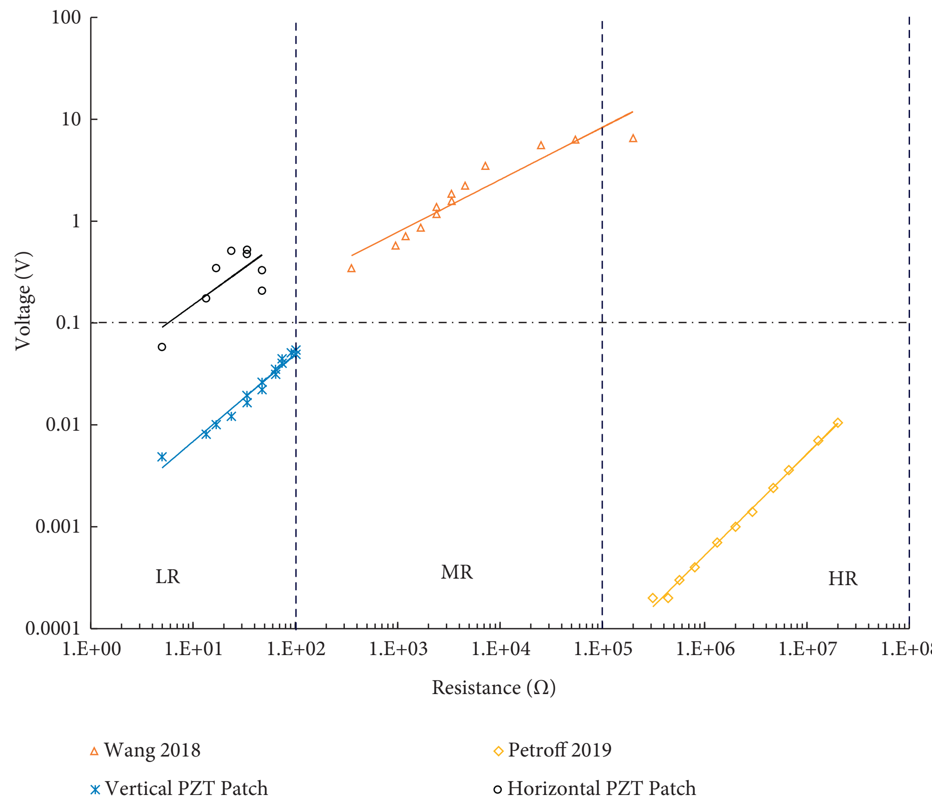

(a)

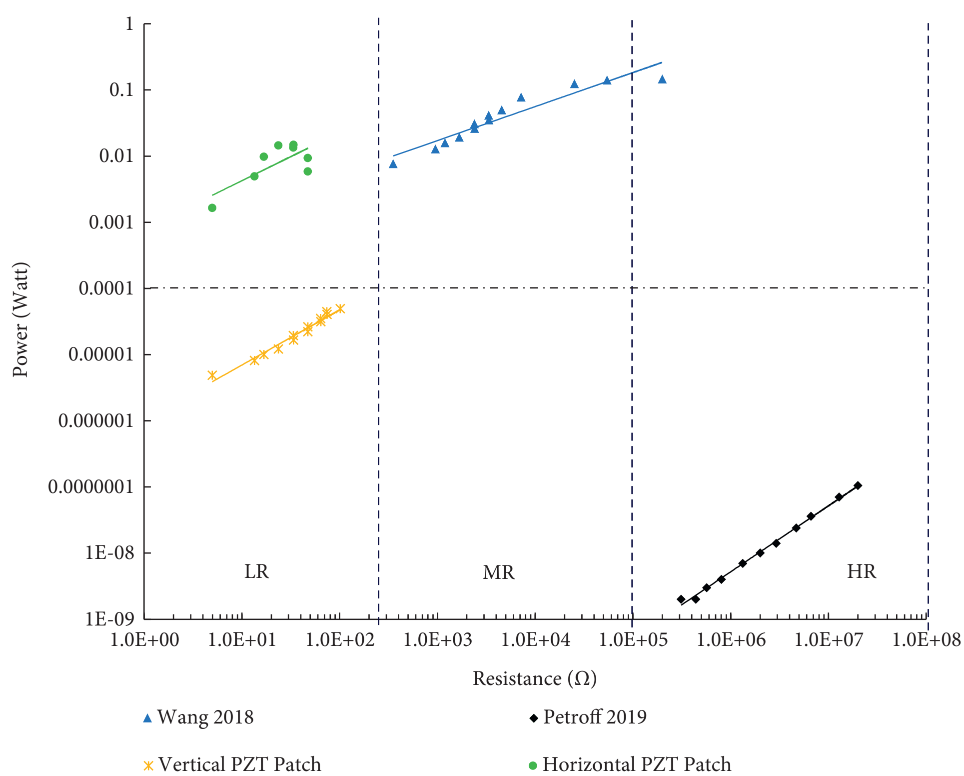

(b)

FIGURE 22: (a) The output voltage for different external resistances for high, medium, and low resistance applications. (b) Power output for different external resistances for high-, medium-, and low-resistance applications.

Table 3: Charge density for confined granular fill with PZT patches.

Alignment of the PZT patch	Maximum charge density at the top surface (Coulombs/m^2)						Maximum charge density at the bottom surface (Coulombs/m^2)					
	H	SH	S	H	SH	S	H	SH	S	H	SH	S
	$0.10 \leq \mu \leq 0.20$			$0.01 \leq \mu \leq 0.08$			$0.10 \leq \mu \leq 0.20$			$0.01 \leq \mu \leq 0.08$		
Horizontal	−26	−256	−5	−12	−15	−20	0	0	0	0	0	0
PZT	0	0	0	0	0	0	+1080	+1300	+1680	+1200	+1480	+1700
Vertical	−3	−30	−40	−104	−125	−166	0	0	0	+280	-100	+480
PZT	0	0	0	+25	+30	+38	+100	+150	+200	-100	+360	-160

Table 4: Voltage output for various PZT patches.

Type of the PZT patch	Maximum voltage output for horizontally embedded PZT patch (Volt)	Maximum voltage output for vertically embedded PZT patch (Volt)	Difference (%)
Hard (H)	0.44	0.05	159.18
Semihard (SH)	0.56	0.06	161.29
Soft (S)	0.33	0.04	156.75

Table 5: Classification of *PZT* applications for output voltage and resistance.

Description	ξ	η	Output voltage (Volt)	Resistance (Ω)	Classification
A flexible piezoelectric energy harvester[a]	5E-10	0.996	10^{-4}–10^{-1}	10^{8}–10^{5}	High-resistance applications (HRA)
A two-degree freedom system with the piezoelectric element[b]	0.0224	0.514	10^{-1}–10^{1}	10^{5}–10^{2}	Medium-resistance applications (MRA)
Horizontally embedded PZT patch[c]	0.001	0.8561	10^{-1}–1	10^{2}–1	Low-resistance applications (LRA)
Vertically embedded PZT patch[d]	0.0282	0.7274	10^{-3}–10^{-1}	10^{2}–1	Low-resistance applications (LRA)

[a]Petroff et al. [42]; [b]Wang et al. [13]; [c, d]present study.

patch, thickness ratio, and material properties. The polarization of the *PZT* patch depends on the piezoelectric strain and the relative permittivity of the *PZT* material. The comparison of the voltage output of the hard, semihard, and soft PZT patches is shown in Figures 20 and 21. As the thickness of the retaining wall increases, the voltage output increases up to a critical thickness ratio. A critical thickness ratio is defined as a ratio of the thickness of the granular fill to that of *PZT* patch at which the maximum energy is harvested.

Figures 20–21 show a graphical representation of the voltage output at various thickness ratios. The semihard *PZT* patch shows the highest voltage output due to the highest polarization ratio of 0.114. At the critical thickness ratios of 0.2 and 0.4, the maximum voltage is obtained for horizontally and vertically aligned patches, respectively, as shown in Table 4. The maximum voltage output observed for horizontally embedded patches is 0.44, 0.56, and 0.33 volt. Similarly, for vertically embedded *PZT* patch voltage output is 0.05, 0.06, and 0.04 volt for hard, semihard, and soft *PZT* patches, respectively. The variation in output voltage indicates that interaction between the *PZT* patch and the retaining wall strongly influences the energy output from the confined granular fill.

4.3. Effect of External Resistance on Power Output of the PZT Patch. This section shows the effect of external resistance on the voltage and power output of the *PZT* patch as per its alignment in the granular fill. Figure 22(a) shows the magnitude of voltage output for the different external resistances. The magnitude of voltage increases logarithmically until a peak voltage of 56 mV for the horizontally embedded *PZT* patch and 6 μV for the vertically embedded *PZT* patch. The magnitude of the voltage output from experimental data from Wang et al. [13] and Petroff et al. [42] is appropriate for MRA and HRA, respectively. Eq. (26) shows a generalized relationship for the output voltage based upon a set of design parameters considered by the present study. An empirical relationship of output voltage for high, medium, and low resistance applications for varying design parameters is expressed as

$$V = \xi R^{\eta}. \tag{26}$$

The variables ξ and η depend upon the design parameters, namely polarization, modulus ratio, position of the *PZT* patch, strain, geometrical, and engineering properties of the confined granular fill and retaining structure. The response of the *PZT* patch can be optimized by changing the design parameters and mechanical properties. Table 5 shows the classification of the application of *PZT* patches based on the voltage output for external resistance. Based on the range of external resistance, the applications of *PZT* patches are classified as low resistance, medium resistance, and high resistance applications.

Figure 22(b) illustrates the magnitude of the power of the present work, and experiment results from the literature are plotted with high medium and low resistance applications. The higher power output is observed for the horizontally embedded *PZT* patch for the same range of the external resistance. The alignment of the *PZT* patch significantly affects the voltage and power output due to the vertical and lateral vibrations due to dynamic loads.

5. Conclusion

A quantitative estimate of piezoelectric voltage output depends upon the stress-strain response of confined granular fill, retaining structure, and *PZT* patches. The stress distribution in the embedded *PZT* patch is affected by the alignment, thickness, and modulus of the material. Three types of PZT patches, namely hard, semihard, and soft *PZT* patches, have been considered to evaluate charge density and voltage output. The conclusions of this study are summarized as follows:

(i) The charge density is significantly affected by the parameters, namely modulus ratio, the magnitude of strain, placement of *PZT* patch, relative permittivity, and polarization of the *PZT* patch.

(ii) Once the *PZT* patches are embedded horizontally, the maximum charge density is observed to be more than three times compared to the vertically embedded *PZT* patches for a set of numerical parameters.

(iii) The maximum voltage output was obtained for the thickness ratio of 0.2–0.6. The voltage output for the horizontally and vertically embedded hard, semihard, and soft PZT patches is obtained in the range of 0.01–0.5 volts and 0.001–0.06 volts, respectively.

(iv) The magnitude of voltage increases logarithmically until a peak voltage of 56 mV for the horizontally embedded *PZT* patch and 6 μV for the vertically embedded *PZT* patch.

(v) A relationship for voltage and power output has been proposed for wide-ranging engineering implements classified as low (LRA), medium (MRA), and high (HRA) resistance applications.

This study considers a comprehensive set of design parameters for selecting *PZT* patches for the voltage output. It provides a framework for evaluating power outputs from confined granular fill and improving the conversion efficiency from the strain fluctuations, polarization per unit permittivity, and geometric properties, which play a significant role in the structural health monitoring of the pavement and retaining structures. The observed voltage output is found appropriate for wide-ranging resistance applications. It is proposed to be up-scaled using multiple patches embedded throughout the confined granular fill subjected to continuous dynamic loads.

Abbreviations

PZT: Lead zirconate titanate
ε_{HE}: Strain in horizontally embedded PZT patch
σ_{PZT}: The stress in the PZT patch
σ_{HE}: Stress in horizontally embedded PZT patch
ε_{VE}: Strain in vertically embedded PZT patch
ρ_{Top}, ρ_{Bottom}: Charge density at the top and bottom surfaces of the *PZT* patch, respectively
$\rho_{\text{THE}}, \rho_{\text{BHE}}$: Charge density at the top and bottom surfaces of the horizontally embedded PZT patch, respectively
Q_{Top}, Q_{Bottom}: Charge quantity at the top and bottom surfaces of the PZT patch, respectively
$Q_{\text{THE}}, Q_{\text{BHE}}$: Charge quantity at the top and bottom surfaces of the horizontally embedded PZT patch, respectively
$\rho_{\text{TVE}}, \rho_{\text{BVE}}$: Charge density function at the top and bottom surfaces of the vertically embedded PZT patch, respectively
$Q_{\text{TVE}}, Q_{\text{BVE}}$: Charge quantity at the top and bottom surfaces of the vertically embedded PZT patch, respectively
h_w: Thickness of the wall
μ: Thickness ratio of PZT patch and backfill (h_P/h_R)
a: The thickness ratio of the retaining wall and PZT patch (h_w/h_P)
b: The modulus ratio of retaining wall and PZT patch (E_w/E_P)
$D3$: Electric displacement
$\varepsilon_{33}^T/\varepsilon_o$: Relative permittivity
ε_0: The absolute permittivity of the vacuum
ε_{33}^T: The permittivity of the material in direction-33 under constant stress
$\varepsilon_{33}^{T=0}$: The free permittivity of the material in direction-33 under no stress
d31: Piezoelectric strain constant in the mode 31
d33: Piezoelectric strain constant in the mode 33
d: Depth of embedment of PZT patch
z: The thickness direction coordinate from the neutral plane
e: Distance between the neutral axis and lower surface of the PZT patch
E: Equivalent electric field intensity
K: Constant of proportionality
VE: Subscript for vertically embedded patch
HE: Subscript for horizontally embedded patch
EP: Modulus of the PZT patch
EW: Modulus of the retaining wall
H: Height of the retaining structure
L: Length of the retaining structure
hP: Thickness of the PZT patch
hR: Thickness of the granular backfill
n : Modulus ratio of *PZT* patch and backfill (E_P/E_R)

V_{HE}: The voltage output for horizontally embedded *PZT* patch
V_{VE}: The voltage output for vertically embedded PZT patch

Appendix

Derivation of Equations for Stress Strain, Charge Density, and Voltage Output of *PZT* Patch

Stress-Strain Analysis for PZT Patch. The stress of confined granular fill is a product of the strain and Young's modulus of the material of the layer. The strain in *PZT* and granular fill depends on the location of the neutral surface [52] of the composite structure; thus, the magnitude of stress strain is expressed as

$$\sigma_z = E_i \varepsilon_z, \varepsilon_z = \frac{z}{R}. \tag{A.1}$$

The relation between the radius of curvature due to small deformation in the layer and stress is expressed as

$$\frac{1}{R} = \frac{M}{EI}, M = -\iint_A z\sigma\, dA, I = \iint_A z^2 \mathrm{d}A, \tag{A.2}$$

where I is the moment of inertia of the composite structure with *PZT* patches and M is the bending moment.

The moment of inertia of the retaining structure is expressed as a composite beam [52]. From equations (A.1) and (A.2), the strain is expressed as

$$\varepsilon_z = \frac{M_z z}{E_i I}. \tag{A.3}$$

The average strain in the middle surface of the vertically embedded *PZT* patch is expressed as

$$\varepsilon_{VE} = \frac{M\left(\overline{z} - z_p\right)}{E_p I_p + E_R I_R + E_w I_w}, \tag{A.4}$$

where $\overline{z} = \sum A_i z_i / \sum A_i$, and $E_w = bE_p$, $h_w = ah_p$, and the neutral surface location of the confined granular fill and retaining structure is expressed as

$$\left(\overline{z} - z_p\right) = \frac{h_s\left(3\mu + 2 - 12a^2 b\mu^2 n\right)}{24\mu n(ab + 1) + 1}, \tag{A.5}$$

$$\varepsilon_{VE} = \frac{M}{E_s H}\left[\frac{\left(\overline{z} - z_p\right)}{\left\{nh_p^3/12\left(1 + ba^3\right) + h_s^3/36\right\} + \left(\overline{z} - z_p\right)^2\left\{nh_p(1 + ab) + h_s/2\right\}}\right], \tag{A.6}$$

where μ is the ratio of the thickness of *PZT* to the backfill (h_P/h_R), n is the ratio of the modulus of the *PZT* patch and the backfill (E_P/E_R), a is the thickness ratio of retaining wall and *PZT* patch (h_w/h_P), and b is the modulus ratio of retaining wall and *PZT* patch (E_w/E_P).

From equations (A.1) and (A.6), the total stress on the *PZT* patch is expressed as

$$\sigma_{VE} = \frac{ME_p}{E_s H}\left[\frac{\left(\overline{z} - z_p\right)}{\left\{nh_p^3/12\left(1 + ba^3\right) + h_s^3/36\right\} + \left(\overline{z} - z_p\right)^2\left\{nh_p(1 + ab) + h_s/2\right\}}\right]. \tag{A.7}$$

Similarly, the average strain can be calculated for the horizontal embedded *PZT* patch.

Charge Density and Voltage. The electromechanical piezoelectric coupling constitutive equation [49] is expressed as

$$D_3 = d_{31}\sigma_{PZT} + \varepsilon_{33}^T E_3. \tag{A.8}$$

According to the stress relationship equation (A.1), the piezoelectric coupling constitutive equation, when the external applied electrical energy is zero ($E_3 = 0$), the lateral electric displacement of the top and bottom surfaces of the *PZT* patch [53], the charge density is expressed as

$$\rho_{\mathrm{Top}} = D_3\left(x, e + h_P\right) = d_{31}\sigma_{PZT}, \tag{A.9}$$

where h_P is the thickness of the *PZT* patch, e is the distance between the neutral plane and interface of the *PZT* patch and granular fill, d_{31} is the piezoelectric strain constant, and σ_{PZT} is average stress on the surface of the *PZT* patch (equation (A.1)). The total quantity of the charge on the top surface of the *PZT* patch has been evaluated by integrating equation (A.2) as

$$Q_{\mathrm{Top}} = \int_0^L bD_3\left(x, e + h_P\right)\mathrm{d}x. \tag{A.10}$$

Similarly, the charge density (equation (A.4)) and total charge quantity on the bottom surface (equation (A.5)) are expressed as

$$\rho_{\text{Bottom}} = -D_3(x, e) = d_{31}\sigma_{PZT}. \tag{A.11}$$

$$Q_{\text{Bottom}} = \int_0^L bD_3(x, e)\mathrm{d}x. \tag{A.12}$$

Thus, by calculating the total charge quantity due to stress on the surface of the *PZT* patch, the open-circuit voltage between the top and bottom surfaces is expressed as

$$V = \int_e^{e+\delta} E(x, z)\mathrm{d}z = \frac{1/2h_P\left(\left|Q_{\text{Top}}\right| + \left|Q_{\text{Bottom}}\right|\right)}{bL\left(\varepsilon_{33}^T/\varepsilon_o\right)}. \tag{A.13}$$

where $\varepsilon_{33}^T/\varepsilon_o$ is the relative permittivity of the piezoelectric material.

Data Availability

All data, models, and code generated or used during the study are included within the article.

Conflicts of Interest

The authors declare that they have no conflicts of interest.

Acknowledgments

The financial support received under the research project entitled "Energy Harvesting through Mechanical Vibrations Generated in Retaining Structure" (grant: F. No. DTU/IRD/619/2105) of Delhi Technological University, Delhi, is thankfully acknowledged.

References

[1] A. García-Olivares, J. Solé, and O. Osychenko, "Transportation in a 100% renewable energy system," *Energy Conversion and Management*, vol. 158, pp. 266–285, 2018.
[2] S. R. Anton and H. A. Sodano, "A review of power harvesting using piezoelectric materials (2003-2006)," *Smart Materials and Structures*, vol. 16, no. 3, pp. R1–R21, 2007.
[3] V. Singh, D. Meena, H. Sharma, A. Trivedi, and B. Singh, "Investigating the role of chalcogen atom in the piezoelectric performance of PVDF/TMDCs based flexible nanogenerator," *Energy*, vol. 239, Article ID 122125, 2022.
[4] S. D. Bahador and Y. Yaowen, "Monitoring hydration of concrete with piezoelectric transducers," in *Proceedings of the 35th Conference on Our World in Concrete & Structures*, Singapore, Octomber 2010.
[5] B. Xu, T. Zhang, G. Song, and H. Gu, "Active interface debonding detection of a concrete-filled steel tube with piezoelectric technologies using wavelet packet analysis," *Mechanical Systems and Signal Processing*, vol. 36, no. 1, pp. 7–17, 2013.
[6] D. Xu, S. Banerjee, Y. Wang, S. Huang, and X. Cheng, "Temperature and loading effects of embedded smart piezoelectric sensor for health monitoring of concrete structures," *Construction and Building Materials*, vol. 76, pp. 187–193, 2015.
[7] A. Erturk and D. J. Inman, "On mechanical modeling of cantilevered piezoelectric vibration energy harvesters," *Journal of Intelligent Material Systems and Structures*, vol. 19, no. 11, pp. 1311–1325, 2008.
[8] H. A. Sodano, D. J. Inman, and G. Park, "A review of power harvesting from vibration using piezoelectric materials," *The Shock and Vibration Digest*, vol. 36, no. 3, pp. 197–205, 2004.
[9] S. P. Beeby, M. J. Tudor, and N. M. White, "Energy harvesting vibration sources for microsystems applications," *Measurement Science and Technology*, vol. 17, no. 12, pp. R175–R195, 2006.
[10] A. Erturk, "Piezoelectric energy harvesting for civil infrastructure system applications: moving loads and surface strain fluctuations," *Journal of Intelligent Material Systems and Structures*, vol. 22, no. 17, pp. 1959–1973, 2011.
[11] M. Rhimi and N. Lajnef, "Tunable energy harvesting from ambient vibrations in civil structures," *Journal of Energy Engineering*, vol. 138, no. 4, pp. 185–193, 2012.
[12] P. Cahill, A. Mathewson, and V. Pakrashi, "Experimental validation of piezoelectric energy-harvesting device for built infrastructure applications," *Journal of Bridge Engineering*, vol. 23, no. 8, Article ID 04018056, 2018.
[13] D. W. Wang, J. L. Mo, X. F. Wang, H. Ouyang, and Z. R. Zhou, "Experimental and numerical investigations of the piezoelectric energy harvesting via friction-induced vibration," *Energy Conversion and Management*, vol. 171, pp. 1134–1149, 2018.
[14] H. Roshani, P. Jagtap, S. Dessouky, A. Montoya, and A. T. Papagiannakis, "Theoretical and experimental evaluation of two roadway piezoelectric-based energy-harvesting prototypes," *Journal of Materials in Civil Engineering*, vol. 30, no. 2, Article ID 04017264, 2017.
[15] F. Chen, R. Balieu, E. Córdoba, and N. Kringos, "Towards an understanding of the structural performance of future electrified roads: a finite element simulation study," *International Journal of Pavement Engineering*, vol. 20, no. 2, pp. 204–215, 2019.
[16] P. Liu, Q. Zhao, H. Yang et al., "Numerical study on influence of piezoelectric energy harvester on asphalt pavement structural responses," *Journal of Materials in Civil Engineering*, vol. 31, Article ID 04019008, 2019.
[17] L. Guo and Q. Lu, "Modeling a new energy harvesting pavement system with experimental verification," *Applied Energy*, vol. 208, pp. 1071–1082, 2017.
[18] H. Yang, Q. Zhao, X. Guo, W. Zhang, P. Liu, and L. Wang, "Numerical analysis of signal response characteristic of piezoelectric energy harvesters embedded in pavement," *Materials*, vol. 13, no. 12, p. 2770, 2020.
[19] H. Roshani and S. Dessouky, "Feasibility Study to Harvest Electric Power from Highway Pavements Using Laboratory Investigation," *Department of Civil and Environmental Engineering University of Texas at San Antonio*, 2015.
[20] D. Hill, A. Agrawal, and N. Tong, *Assessment of Piezoelectric Materials for Roadway Energy Harvesting, Report Prepared by DNV KEMA Energy and Sustainability Inc. For the California Energy Commission*, KEMA, Mumbai, 2013.
[21] L. Guo and Q. Lu, "Potentials of piezoelectric and thermoelectric technologies for harvesting energy from pavements," *Renewable and Sustainable Energy Reviews*, vol. 72, pp. 761–773, 2017.
[22] Y. Yang, Q. Shen, J. Jin, Y. Wang, W. Qian, and D. Yuan, "Rotational piezoelectric wind energy harvesting using

impact-induced resonance," *Applied Physics Letters*, vol. 105, no. 5, Article ID 053901, 2014.

[23] N. Rezaei-Hosseinabadi, A. Tabesh, R. Dehghani, and A. Aghili, "An efficient piezoelectric windmill topology for energy harvesting from low-speed air flows," *IEEE Ind. Electron. Mag.*vol. 62, no. 6, pp. 3576–3583, 2014.

[24] V. C. Sousa, M. de M Anicézio, C. De Marqui, and A. Erturk, "Enhanced aeroelastic energy harvesting by exploiting combined nonlinearities: theory and experiment," *Smart Materials and Structures*, vol. 20, no. 9, Article ID 094007, 2011.

[25] R. Murray and J. Rastegar, "Novel two-stage piezoelectric-based ocean wave energy harvesters for moored or unmoored buoys," *Int. Soc. Opt. Eng.*vol. 7288, Article ID 72880E, 2009.

[26] K. A. Cunefare, E. A. Skow, A. Erturk, J. Savor, N. Verma, and M. R. Cacan, "Energy harvesting fro m hydraulic pressure fluctuations," *Smart Materials and Structures*, vol. 22, no. 2, Article ID 025036, 2013.

[27] X. D. Xie, Q. Wang, and S. J. Wang, "Energy harvesting from high-rise buildings by a piezoelectric harvester device," *Energy*, vol. 93, pp. 1345–1352, 2015.

[28] X. Li and V. Strezov, "Modelling piezoelectric energy harvesting potential in an educational building," *Energy Conversion and Management*, vol. 85, pp. 435–442, 2014.

[29] S. W. Kim, B. G. Jeon, N. S. Kim, and J. C. Park, "Vision-based monitoring system for evaluating cable tensile forces on a cable-stayed bridge," *Structural Health Monitoring*, vol. 12, no. 5-6, pp. 440–456, 2013.

[30] Ö. Zorlu, E. T. Topal, and H. Külah, "A vibration-based electromagnetic energy harvester using mechanical frequency up-conversion method," *IEEE Sensors Journal*, vol. 11, no. 2, pp. 481–488, 2010.

[31] S. P. Beeby, R. N. Torah, M. J. Tudor et al., "A micro electromagnetic generator for vibration energy harvesting," *Journal of Micromechanics and Microengineering*, vol. 17, no. 7, pp. 1257–1265, 2007.

[32] K. Sasaki, Y. Osaki, J. Okazaki, H. Hosaka, and K. Itao, "Vibration-based automatic power-generation system," *Microsystem Technologies*, vol. 11, no. 8, pp. 965–969, 2005.

[33] P. Glynne-Jones, M. J. Tudor, S. P. Beeby, and N. M. White, "An electromagnetic, vibration-powered generator for intelligent sensor systems," *Sensors Actuators, A Phys.*vol. 110, no. 1-3, pp. 344–349, 2004.

[34] H. Wang, A. Jasim, and X. Chen, "Energy harvesting technologies in roadway and bridge for different applications–A comprehensive review," *Applied Energy*, vol. 212, pp. 1083–1094, 2018.

[35] Z. Jiang, J. Cai, and P. S. Moses, "Smoothing control of solar photovoltaic generation using building thermal loads," *Applied Energy*, vol. 277, Article ID 115523, 2020.

[36] A. Zahedi, "Solar photovoltaic (PV) energy; latest developments in the building integrated and hybrid PV systems," *Renewable Energy*, vol. 31, no. 5, pp. 711–718, 2006.

[37] T. Nordmann, A. Froelich, A. Goetzberger et al., "The potential of PV noise barrier technology in Europe," in *Sixteenth European Photovoltaic Solar Energy Conference*, pp. 2912–2916, Routledge, Milton Park, Abingdon-on-Thames, 2020.

[38] F. Chen, N. Taylor, R. Balieu, and N. Kringos, "Dynamic application of the Inductive Power Transfer (IPT) systems in an electrified road: dielectric power loss due to pavement materials," *Construction and Building Materials*, vol. 147, pp. 9–16, 2017.

[39] H. Zhao, J. Ling, and J. Yu, "A comparative analysis of piezoelectric transducers for harvesting energy from asphalt pavement," *Journal of the Ceramic Society of Japan*, vol. 120, no. 1404, pp. 317–323, 2012.

[40] X. Ren, "Large electric-field-induced strain in ferroelectric crystals by point-defect-mediated reversible domain switching," *Nature Materials*, vol. 3, no. 2, pp. 91–94, 2004.

[41] B. Singh, D. Varandani, and B. R. Mehta, "Effect of conductive atomic force microscope tip loading force on tip-sample interface electronic characteristics: unipolar to bipolar resistive switching transition," *Applied Physics Letters*, vol. 103, no. 5, Article ID 051604, 2013.

[42] C. A. Petroff, T. F. Bina, and G. R. Hutchison, "Highly tunable molecularly doped flexible poly(dimethylsiloxane) foam piezoelectric energy harvesters," *ACS Applied Energy Materials*, vol. 2, no. 9, pp. 6484–6489, 2019.

[43] Physik Instrumente (Pi) GmbH, "Co. KG," *CAT 125E R3 Piezoelectric Ceramic Products*, Karlsruhe, Germany, 2011.

[44] R. A. Islam and S. Priya, "Realization of high-energy density polycrystalline piezoelectric ceramics," *Applied Physics Letters*, vol. 88, no. 3, Article ID 032903, 2006.

[45] N. Kumari and A. Trivedi, "Application of semi-active control strategy for the wall retaining granular fills," *Springer Series in Geomechanics and Geoengineering*, vol. 13, pp. 978–982, 2018.

[46] N. Kumari and A. Trivedi, "Vibration control of flexible retention systems," *Lecture Notes in Civil Engineering*, Springer, no. 56, , pp. 529–539, Singapore, 2020.

[47] G. Park, T. Rosing, M. D. Todd, C. R. Farrar, and W. Hodgkiss, "Energy harvesting for structural health monitoring sensor networks," *Journal of Infrastructure Systems*, vol. 14, no. 1, pp. 64–79, 2008.

[48] L. Mateu and F. Moll, "Review of energy harvesting techniques and applications for microelectronics," *VLSI Circuits and Systems II*, vol. 5837, pp. 359–374, 2005.

[49] A. Meitzler, H. Tiersten, A. Warner, D. Berlincourt, G. Couqin, and F. Welsh, *IEEE Standard on Piezoelectricity*, pp. 176–1987, IEEE Ultrasonics, Ferroelectrics, and Frequency Control Society, Metropolitan Area, France, 1988.

[50] Y. Amini, M. Heshmati, P. Fatehi, and S. E. Habibi, "Energy harvesting from vibrations of a functionally graded beam due to moving loads and moving masses," *Journal of Engineering Mechanics*, vol. 143, no. 9, Article ID 04017063, 2017.

[51] I. Chopra, "Review of state of art of smart structures and integrated systems," *AIAA Journal*, vol. 40, no. 11, pp. 2145–2187, 2002.

[52] M. Kerboua, M. Benguediab, A. A.Megnounif, K. H. Benrahou, and F. Kaoulala, "Semi active control of civil structures, analytical and numerical studies," *Physics Procedia*, vol. 55, pp. 301–306, 2014.

[53] G. Zhang, S. Gao, and H. Liu, "A utility piezoelectric energy harvester with low frequency and high-output voltage: theoretical model, experimental verification and energy storage," *AIP Advances*, vol. 6, no. 9, Article ID 095208, 2016.